The Creston, California, meteorite fall and the origin of L chondrites

Peter JENNISKENS [1,2]*, Jason UTAS [3], Qing-Zhu YIN [4], Robert D. MATSON[5],
Marc FRIES [6], J. Andreas HOWELL [7], Dwayne FREE [7], Jim ALBERS[1],
Hadrien DEVILLEPOIX [8], Phil BLAND [8], Aaron MILLER[9], Robert VERISH[10],
Laurence A. J. GARVIE [11], Michael E. ZOLENSKY[6], Karen ZIEGLER [12],
Matthew E. SANBORN [4], Kenneth L. VEROSUB[4], Douglas J. ROWLAND [13],
Daniel R. OSTROWSKI [2,14], Kathryn BRYSON [2,14], Matthias LAUBENSTEIN [15],
Qin ZHOU [16], Qiu-Li LI [17], Xian-Hua LI [17], Yu LIU [17], Guo-Qiang TANG [17],
Kees WELTEN [18], Marc W. CAFFEE[19], Matthias M. M. MEIER [20], Amy A. PLANT [20],
Colin MADEN [20], Henner BUSEMANN [20], Mikael GRANVIK [21,22]
(The Creston Meteorite Consortium)

[1]SETI Institute, Carl Sagan Center, Mountain View, California 94043, USA
[2]NASA Ames Research Center, Moffett Field, California 94035, USA
[3]Institute of Geophysics and Planetary Physics, UCLA, Los Angeles, California 90095, USA
[4]Department of Earth and Planetary Sciences, University of California at Davis, Davis, California 95616, USA
[5]Leidos, Seal Beach, San Diego, California 90704, USA
[6]Astromaterials Research and Exploration Science, NASA Johnson Space Center, Houston, Texas 77058, USA
[7]Spalding Allsky Camera Network, SkySentinel, LLC (SSL), Melbourne, Florida 32940, USA
[8]Faculty of Science & Engineering, Curtin University, Bentley, Perth, Western Australia 6102, Australia
[9]Ancient Earth Trading Co., Atascadero, California 93423, USA
[10]Meteorite Recovery Lab, Escondido, California 92046, USA
[11]Center for Meteorite Studies, School of Earth & Space Exploration, Arizona State University, Tempe, Arizona 85287, USA
[12]Institute of Meteoritics, University of New Mexico, Albuquerque, New Mexico 87131, USA
[13]Center for Molecular and Genomic Imaging, Department of Biomedical Engineering, UC Davis, Davis, California 95616, USA
[14]Bay Area Environmental Research Institute, 625 2nd St., Suite 209, Petaluma, California 94952, USA
[15]Ist. Naz. di Fiscia Nucleare, Lab. Naz. del Gran Sasso, I-67100 Assergi (AQ), Italy
[16]National Astronomical Observatories, Chinese Academy of Sciences, Beijing 100012, China
[17]State Key Laboratory of Lithospheric Evolution, Inst. Geol. and Geophys., Chinese Acad. Sci., Beijing 100029, China
[18]Space Sciences Laboratory, University of California, Berkeley, California 94720, USA
[19]PRIME Laboratory, Purdue University, West Lafayette, Indiana 47907, USA
[20]Institute of Geochemistry and Petrology, ETH Zürich, CH-8092, Zürich, Switzerland
[21]University of Helsinki, Department of Physics, FI-00014, Helsinki, Finland
[22]Luleå University of Technology, Division of Space Technology, S-98128 Kiruna, Sweden
*Corresponding author. E-mail: petrus.m.jenniskens@nasa.gov

Abstract–It has been proposed that all L chondrites resulted from an ongoing collisional cascade of fragments that originated from the formation of the ~500 Ma old asteroid family Gefion, located near the 5:2 mean-motion resonance with Jupiter in the middle Main Belt. If so, L chondrite pre-atmospheric orbits should be distributed as expected for that source region. Here, we present contradictory results from the orbit and collisional history of the October 24, 2015, L6 ordinary chondrite fall at Creston, CA (here reclassified to L5/6). Creston's short 1.30 ± 0.02 AU semimajor axis orbit would imply a long dynamical evolution if it originated from the middle Main Belt. Indeed, Creston has a high cosmic ray exposure age of 40–50 Ma. However, Creston's small meteoroid size and low $4.23 \pm 0.07°$ inclination indicate a short dynamical lifetime against collisions. This suggests, instead, that Creston originated most likely in the inner asteroid belt and was delivered via the ν_6 resonance. The U-Pb systematics of Creston apatite reveals a Pb-Pb age of

4,497.1 ± 3.7 Ma, and an upper intercept U-Pb age of 4,496.7 ± 5.8 Ma (2σ), circa 70 Ma after formation of CAI, as found for other L chondrites. The K-Ar (age ~4.3 Ga) and U,Th-He (age ~1 Ga) chronometers were not reset at ~500 Ma, while the lower intercept U-Pb age is poorly defined as 770 ± 320 Ma. So far, the three known L chondrites that impacted on orbits with semimajor axes a <2.0 AU all have high (>3 Ga) K-Ar ages. This argues for a source of some of our L chondrites in the inner Main Belt. Not all L chondrites originate in a continuous population of Gefion family debris stretching across the 3:1 mean-motion resonance.

INTRODUCTION

There is an ongoing effort to identify the source of L chondrites in the asteroid belt. The delivery resonance and inclination of the source region can be identified in a statistical sense from meteorite falls for which an atmospheric impact trajectory and pre-atmospheric orbit are calculated (Jenniskens 2014). So far, five L5 and L6 chondrites have yielded pre-impact orbits: Innisfree, Jesenice, Park Forest, Villalbeto de la Peña, and Novato.

About two-thirds of L chondrites have a common 470 ± 6 Ma Ar-Ar and U-Pb resetting age, especially those that show shock blackening (Anders 1964; Haack et al. 1996; Alexeev 1998; Scott 2002; Korochantseva et al. 2007; Weirich et al. 2012; Yin et al. 2014; Li and Hsu 2016; Wu and Hsu 2017). In addition, L chondrite falls were much more common 470 Ma ago, where they are found in the fossil record of terrestrial strata dated to 467.3 ± 1.6 Ma (Schmitz et al. 2001, 2016).

It has been proposed that the Gefion asteroid family, located near the 5:2 mean-motion resonance, was formed at that time and this is the source of these shocked L chondrites (Nesvorný et al. 2009). While delivery was rapid, initially, via the 5:2 mean-motion resonance, the meteorites would now be delivered to Earth more efficiently via the 3:1 mean-motion resonance. Gefion is the only known family with large members of L (as opposed to H and LL) chondrite composition (Vernazza et al. 2014) and some asteroids found in the 3:1 mean-motion resonance, e.g., (355) Gabriella, (14470) Utra, and (1722) Goffin, have L chondrite-like spectra (Fieber-Beyer and Gaffey 2015). In more recent years, however, the reflection spectra of some Gefion family members were found to resemble that of H chondrites and basaltic achondrites (McGraw et al. 2017) and the age of the Gefion family may be older than required, 1103 ± 386 Ma according to Spoto et al. (2015), who did not include the initial velocity at ejection, however.

There could be more than one source region of L chondrites in the main asteroid belt. It has been argued that large groups of compositionally similar asteroids are a natural outcome of planetesimal formation (Youdin 2011; Vernazza et al. 2014). Also, the current asteroid population is mostly composed of reassembled matter from large-scale disruptions of an earlier generation of planetesimals (Bottke et al. 2005). If so, the L chondrite parent body may have broken into several daughter asteroids during an initial disruption of the L chondrite parent body long ago, each of which could later have created an asteroid family in a different part of the Main Belt.

More than one recent collision created the meteoroids that now impact Earth. L5 and L6 chondrites have a broad distribution of cosmic ray exposure ages (CRE). The CRE age identifies the moment in time when a collision caused the meteoroid to no longer be shielded from cosmic rays by a few meters of overlaying burden. The broad distribution implies that multiple disruptive collision or cratering events produced this meteorite type (Marti and Graf 1992; Eugster et al. 2006; Wasson 2012). Note that L3 and L4 chondrites appear to have different CRE age distributions than L5 or L6 chondrites, and are not considered here. At this moment, there are no observed L3 or L4 falls with measured pre-atmospheric orbits.

Here, we report on the October 24, 2015 fall of the ordinary chondrite Creston near Paso Robles, California. Two hundred and eighteen eyewitnesses reported the fireball (American Meteor Society event number 2635-2015). Fourteen witnesses close to the path heard sonic booms shortly after the fireball. Seismic stations timed tremors when the shock wave coupled to the ground. Based on the visual and seismic sightings, six Doppler radar returns from the United States National Oceanic and Atmospheric Administration (NOAA) next generation weather radar network (NEXRAD) were identified that were likely from falling meteorites (Fries et al. 2016). Based on the radar-defined search area, the first stone was located on October 27, now named CR01 and classified as an L6 ordinary chondrite (Bouvier et al. 2017). The stone had shattered when it hit a metal fence post. Five other meteorites were found in the following month, with a total weight of 852.3 g (Table 1).

Two of the meteorites (CR05 and CR06) were made available for nondestructive analysis (Fig. 1), while

Table 1. Creston meteorite masses and find locations.

| CR#	Date of find	Mass (g)	Latitude (N)	Longitude (W)	Altitude (m)	Finder
01[b]	October 27, 2015	~396[a]	35.57508	120.49847	397	Robert & Ann Marie Ward
02[b]	October 28, 2015	69.2	~35.568	~120.481	~499	Terry Scott
03	October 31, 2015	102.2	~35.568	~120.481	~499	Terry Scott
04	November 16, 2015	108	~35.568	~120.481	~499	Michael Farmer
05[b]	November 19, 2015	72.681	~35.565	~120.467	~477	(local finder/via Sonny Clary)
06[b]	November 21, 2015	95.549	35.56547	120.46747	477	Aaron Miller

[a]Broken on impact.
[b]Meteorites studied here.
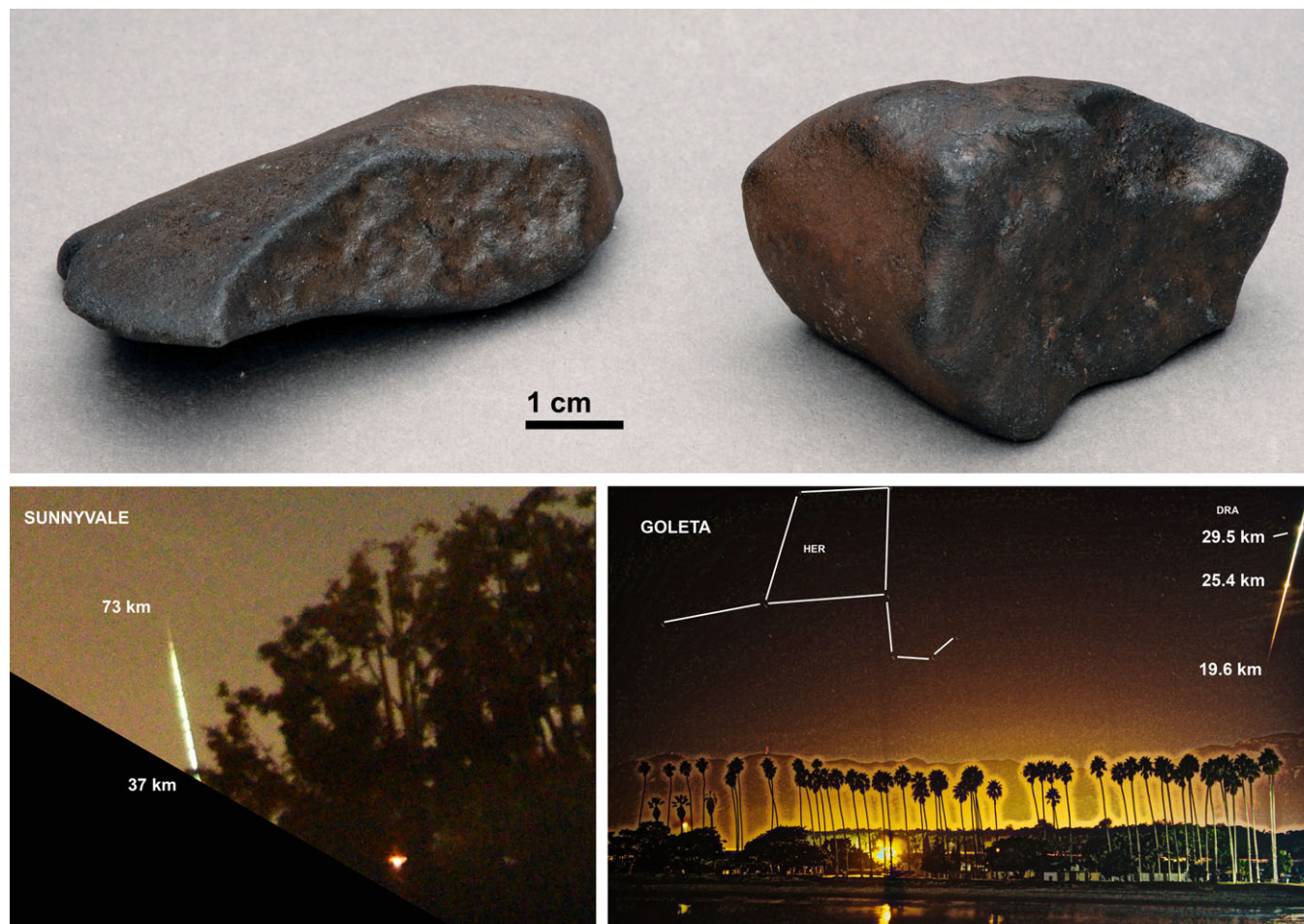
Fig. 1. Top) Optical photographs of Creston meteorites #5 (left) and #6. Notice how each meteorite has one side that is more reddish colored, the irregular surface in the case of C05 and the fresher flatter surface in the case of C06, respectively. Bottom) Creston bolide from Sunnyvale (cropped image) and Goleta.

fragments of meteorites CR01 and CR02 were used for destructive analysis. We determined the pre-atmospheric orbit and the collision history of the meteorites in order to investigate whether Creston originated from the same source as other L chondrites with known pre-atmospheric orbits. We also comprehensively characterized the meteorite mineralogically, petrographically, geochemically, isotopically, and magnetically.

EXPERIMENTAL METHODS

Meteoroid Trajectory and Orbit

The fireball was recorded by an automated digital camera developed for the Desert Fireball Network (DFN) during testing at the Cameras for Allsky Meteor Surveillance project (CAMS; Jenniskens et al. 2011)

station in Sunnyvale, California (Fig. 2). The camera consists of a Nikon D810 digital still camera equipped with a liquid crystal shutter that interupts the image 10 times per second, with some breaks kept dark to encode the time during the exposure (Fig. 1, lower left). At the time of the fall, the skies in Sunnyvale were hazy and illuminated by a full Moon. Few stars are visible in the image. Images from the previous night were used to calibrate the background star field with a mean observed-calculated astrometric precision of O-C = 1.0' (Table 2).

A second digital still image, a single exposure, was obtained from the pier at Goleta by Christian M. Rodriguez of Santa Barbara and posted on a social media website. The meteor is captured near the right edge of the image, entering from a corner (Fig. 1, lower right). Upon

request, the original image was made available for analysis to reveal a rich star field, including a star on the right side of the meteor trail. Rodriguez saw the fireball and stopped the exposure about 5 s after it faded. The field of view is relatively small, resulting in an O-C = 0.24'.

The fireball was also captured in two SkySentinel allsky cameras, one at Riverside, operated by Richard Garcia, and one in El Segundo, operated by Dave Goodyear (Fig. 3). Station locations relative to Sunnyvale and Goleta are shown in Fig. 2. Both cameras are small image format (640 × 480 pixels), low-light video cameras equipped with an allsky lens. In Riverside, there is more obstruction near the horizon than in El Segundo, the latter capturing the same two flares as seen in Goleta. In Riverside, only the first flash
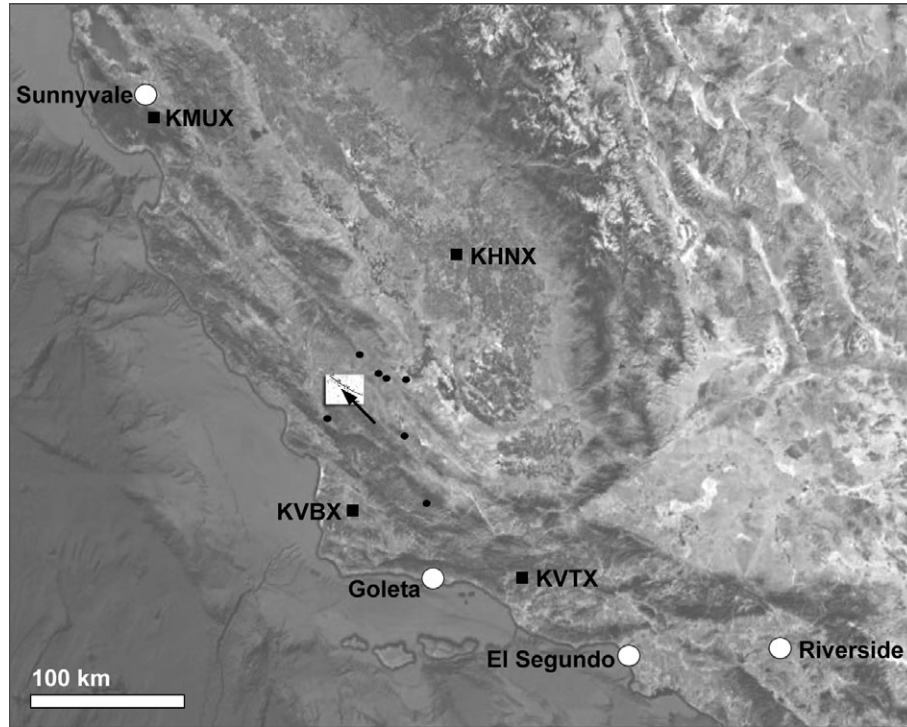

Fig. 2. California map with location of camera stations (open circles), radar stations (black squares), and seismic stations (black dots). (White area is enlarged in Fig. 5.)

Table 2. Camera station locations, sampling rate, and astrometric precision.

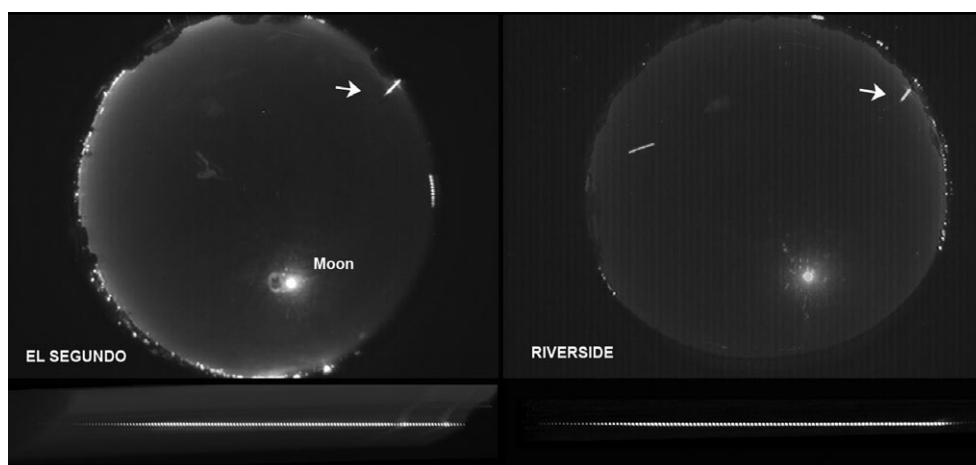| #	Station	Latitude (N)	Longitude (W)	Altitude (m)	Type	Frame rate (Hz)	O-C (′)	Range (km)
1	Sunnyvale	37.34781	122.03896	60	Digital Still w. Shutter	10.00	1.0 ± 0.7	264
2	Goleta	34.41508	119.82893	11	Digital Still	–	0.24 ± 0.14	146
3	Riverside	33.91367	117.34020	471	Allsky Video	29.97	4.4 ± 3.1	331
4	El Segundo	33.92745	118.41215	46	Allsky Video	29.97	4.4 ± 3.3	250

Fig. 3. Creston bolide from (left) El Segundo and (right) Riverside in SkySentinel video. Below each allsky image summary is a sequence of video frames showing the meteor in detail (moving from left to right toward the horizon).

is recorded. The Iris software was used to track the meteor's position and brightness in the video frames. No stars are visible in the individual image frames, but after averaging a number of frames, sufficient stars can be found for calibration above 15° elevation. The zenith angles (z) of the meteor as a function of time were computed from pixel coordinates by fitting the exponential model as a function of zenith distance described in Borovicka et al. (1995). Observed-calculated root-mean-square precision for 82 stars (above 15° elevation) was O-C = 4.4'. This is sufficient to align the observed light curve to the trajectory solution, but not enough to help improve the trajectory solution from combining the Sunnyvale and Goleta observations.

Meteorite Petrography, Bulk Chemistry, and Isotopes

Petrographic analysis of CR01 was done initially at the Arizona State University and reported in Bouvier et al. (2017). At NASA Johnson Space Center (JSC), electron microprobe analysis (EPMA) of a subsample of CR02 was performed to evaluate metamorphic conditions of the rock and verify the initial classification. These analyses were made using a Cameca SX100 microprobe at the E-beam laboratory of the Astromaterials and Exploration Science (ARES) Division of JSC. Natural mineral standards were used, and analytical errors are at the 0.1 wt% level for most elements. We used a 1 μm focused beam in all analyses, at 15 kV and 20 nA. The moderately and highly shocked lithologies were analyzed separately, for comparison.

Oxygen isotope studies were performed at the University of New Mexico. Three subsamples of 1.20, 1.30, and 0.80 mg, respectively, were acid-treated in order to remove any possible terrestrial contamination.

Molecular oxygen was released from the samples by laser-assisted fluorination (20 or 50 W far-infrared CO_2 laser) in a BrF_5-atmosphere, producing molecular O_2 and solid fluorides, from which excess BrF_5 was removed by reaction with hot NaCl. The oxygen was purified by freezing at −196 °C, followed by elution at ~300 °C into a He-stream. NF_3 is then separated in a gas chromatography column and frozen again at −196 °C to remove He. The O_2 is then released directly into a dual inlet mass spectrometer (Thermo Finnigan MAT 253). The San Carlos olivine standards (~1–2 mg) were analyzed daily. Each mass spectroscopic analysis consists of 20 cycles of standard-sample comparisons (e.g., Popova et al. 2013).

Chromium isotope and bulk chemical composition measurements were completed at the University of California, Davis (UC Davis). A fusion crust-free fragment (50.8 mg) was crushed into a powder and placed into a polytetrafluoroethylene (PTFE) Parr capsule along with a 3:1 mixture of concentrated HF: HNO_3 acid. The PTFE capsule was placed into a stainless steel jacket and heated in a 190 °C oven for 96 h. After complete dissolution, an aliquot of the solution was used for Cr isotopes and the remaining solution was used for major, minor, and trace element concentration determination. Chromium was separated from the bulk sample using a three-column chemical separation procedure described previously by Yamakawa et al. (2009). After separating Cr from the sample matrix, the isotopic composition of the purified Cr fraction was analyzed using a Thermo Triton Plus thermal ionization mass spectrometer at UC Davis. A total Cr load of 12 μg was loaded onto four outgassed W filaments (3 μg of Cr per filament). The Cr separated from Creston was bracketed by four filaments loaded with NIST SRM 979 Cr standard solution at the same

total Cr load as the Creston fractions. Chromium isotopic compositions are reported as parts per 10,000 deviation from the measured SRM 979 standard (ε-notation).

An aliquot set aside from the same dissolved sample above before Cr separation was used to determine the concentrations for a suite of elements (major, minor, and trace) using Thermo Element XR high-resolution inductively coupled plasma mass spectrometer at UC Davis. The analytical methods for this procedure have been described previously (Jenniskens et al. 2012, 2014; Popova et al. 2013).

Meteorite Cosmic Ray Exposure, K-Ar and U,Th-He Ages

To determine the cosmic ray exposure age and meteoroid size, cosmogenic radionuclide concentrations were analyzed by means of nondestructive high purity germanium (HPGe) gamma spectroscopy. Two specimens of Creston (CR05 and CR06) were measured in the underground laboratories at the Laboratori Nazionali del Gran Sasso (LNGS) (Arpesella 1996) for 14.74 days (CR06, 263 days after the fall) and 15.90 days (CR05, 278 days after the fall), respectively. The counting efficiencies have been calculated using thoroughly tested Monte Carlo codes.

Additional measurements of cosmogenic radionuclides ^{10}Be and ^{36}Cl were obtained from a sample of CR02 weighting ~52 mg. At UC Berkeley, the sample was gently crushed in an agate mortar and the powder dissolved in concentrated HF/HNO_3 along with a carrier solution containing approximately 2.8 mg of Be and 3.5 mg of Cl. After complete dissolution of the sample, an aliquot was taken for chemical analysis by ICP-OES and radionuclides were separated and purified for measurement by accelerator mass spectroscopy (AMS) at Purdue University.

At ETH Zürich, the CRE age and K-Ar age were determined from noble gas concentrations. Two samples of CR02 were prepared by breaking apart a ~70 mg piece of Creston. The samples were weighed, wrapped in Al foil, and loaded into an in-house built noble gas mass spectrometer. Noble gases were extracted by a furnace heated by electron bombardment to 1700–1800 °C in a single heating step, and separated into a He and Ne, and an Ar fraction by temporarily freezing the Ar to a charcoal cooled by liquid nitrogen. Analysis was done according to a protocol most recently described in Meier et al. (2017). Helium-4 and all Ne and Ar isotopes were measured, together with the ion species H_2O^+, $^{35}Cl^+$, $^{37}Cl^+$, $^{40}Ar^+$, and CO_2^+, which were monitored to potentially correct for interferences on the masses of the noble gas isotopes, but all

interferences proved to be negligible. The two samples were analyzed back-to-back, and bracketed with two Al blanks. Blank contributions to total signals were <0.04% on ^4He, <0.8%, and <4% on all Ne and Ar isotopes, respectively.

Meteorite U-Pb and Pb-Pb Ages

U-Pb ages for Creston were determined at the National Astronomical Observatories (NAO), Chinese Academy of Sciences (CAS) in Beijing. The detailed analytical procedure for U-Pb dating of phosphate grains in terrestrial rocks can be found in Li et al. (2010), which was further refined and applied successfully to meteorites (Popova et al. 2013; Zhou et al. 2013; Yin et al. 2014). Backscattered electron images of phosphate grains in a polished mount of CR01 were imaged with a Carl Zeiss SUPRA-55 field-emission scanning electron microscope (FESEM) equipped with energy dispersive spectrometer (EDS). The probe current was 300 pA at an accelerating voltage of 15 kV. This step was essential in selecting suitable analytical spots in the subsequent ion probe session for U-Pb dating to avoid microfractures, inclusions, and other observed physical defects in the individual phosphate grains. The analytical spots are identified in Fig. 4.

In situ isotopic analysis of U-Pb for phosphate grains was performed on the large radius magnetic sector multicollector, secondary ion mass spectrometer (SIMS), a Cameca IMS-1280HR at the Institute of
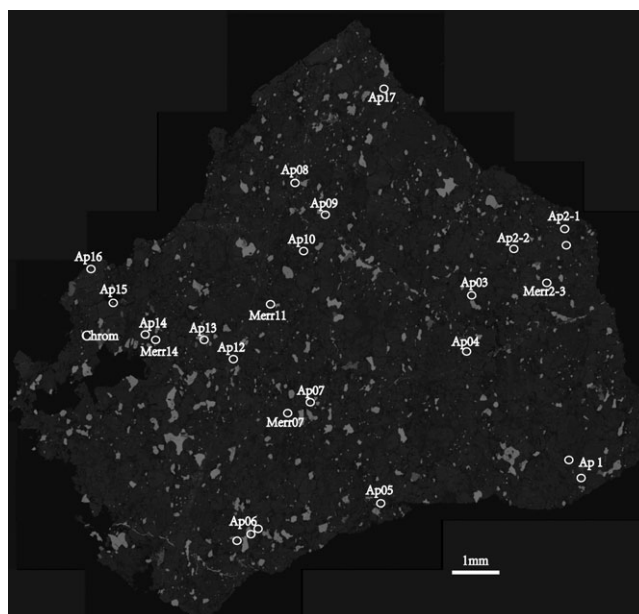

Fig. 4. Apatite grains in Creston CR01. Ap = apatite; Chrom = chromite; Merr = merrillite.

Geology and Geophysics (IGG), Chinese Academy of Sciences (CAS) in Beijing. The O^{2-} primary ion beam was accelerated at -13 kV, with an intensity ranging between 8 and 9 nA. The Köhler illumination mode was used with a 200 mm diameter aperture, resulting in an elliptical spot size of 20×30 mm^2 on the target. Positive secondary ions were extracted with a 10 kV potential. A monocollector electron multiplier (EM) was used as the detection device to measure secondary ion beam intensities of $^{204}Pb^+$, $^{206}Pb^+$, $^{207}Pb^+$, $^{208}Pb^+$, $^{232}Th^+$, $^{238}U^+$, $^{232}Th^{16}O^+$, $^{238}U^{16}O^+$, $^{238}U^{16}O_2^+$, and a matrix reference peak of $^{40}Ca_2^{31}P^{16}O_3^+$ at a mass resolution of approximately 9000 (defined at 50% height). The $^{40}Ca_2^{31}P^{16}O_3^+$ signal was used as reference peak for tuning the secondary ions, energy, and mass adjustments. Pb/U ratios were calibrated with power law relationship between $^{206}Pb^{*+}/^{238}U^+$ and $^{238}U^{16}O_2^+/^{238}U^+$ relative to an apatite standard of NW-1 (1160 Ma) that comes from the same complex at Prairie Lake as that of the Sano et al. (1999) apatite standard (PRAP). Uranium concentration is calibrated relative to the Durango apatite, which contains approximately 9 ppm of U (Trotter and Eggins 2006). The detection limit is approximately 4 ppb of U in apatite. The $^{206}Pb/^{238}U$ standard deviation measured in the standard was propagated to the unknowns. Each measurement consisted of 10 cycles, with the total analytical time of about 23 min. Due to the low uranium concentration, all of the merrillites failed to yield useful Pb-Pb age information. The uncertainties for individual apatite analyses are reported as 1σ. The weighted average of $^{206}Pb^*/^{238}U$ and Pb-Pb ages, quoted at the 95% confidence level, was calculated using ISOPLOT 3.0.

The ^{204}Pb counts are very low in all apatite grains. Most points have zero counts, which indicate the common lead levels are very low. We assumed that the common lead level is mostly surface contamination, and correction

using modern terrestrial common lead composition was applied. Given the very low level of ^{204}Pb and common Pb fraction f_{206} (%), using the primordial lead composition (Tatsumoto et al. 1973) instead of terrestrial common lead would make no difference in the calculated radiogenic lead composition. To illustrate the point, we plotted the common lead corrected data in both the normal Wetherill-type concordia diagram, inverse Tera-Wasserburg diagram, as well as the 3-D linear regression of the total lead as measured (without correction for initial or common lead) in $^{207}Pb/^{206}Pb$ versus $^{238}U/^{206}Pb$ plane (Wendt and Carl 1984; Wendt 1989; Ludwig 1998). The similar results (not shown here) among the three panels within errors indicate that the unknown common Pb isotope composition and its correction are insignificant for age calculations.

RESULTS

Trajectory and Orbit

The exact time of the onset of the fireball was derived from the CAMS low-light video cameras (Jenniskens et al. 2011). GPS synchronization of the DFN camera was unreliable at the time of the event. The fireball was just below the camera field of view at the CAMS station at Fremont Peak Observatory. A single-frame flash (<0.05 s long) was detected in cameras 62, 71, and 73 at 05:47:48.8 ± 0.2 UTC, and a weaker flash at 05:47:49.1 ± 0.2 UTC, which are interpreted to be the two flares seen in Fig. 1.

Results for the trajectory and orbit derived from triangulation of Sunnyvale with Goleta are given in Table 3 and Fig. 5. The convergence angle between the intersecting planes through meteor and station is only 7.2°. The solution based on DFN/Sunnyvale and Goleta is most sensitive to systematic errors in the DFN

Table 3. Trajectory and orbit, October 24, 2015.

| Trajectory (apparent):		Orbit (geocentric):	
Time begin (UT)	05:47:44.3 ± 0.1	Solar longitude (°)	210.2828 ± 0.0001
Right ascension (°, apparent)	25.90 ± 0.07	Right ascension (°, geocentric)	28.50 ± 0.10
Declination (°, apparent)	+4.83 ± 0.10	Declination (°, geocentric)	−0.70 ± 0.18
Entry speed (km/s, apparent)	16.00 ± 0.26	Entry speed (km/s, geocentric)	11.26 ± 0.34
Latitude begin (°, N)	35.347 ± 0.028	Perihelion distance (AU)	0.7670 ± 0.0053
Longitude begin (°, W)	120.226 ± 0.022	Semimajor axis (AU)	1.300 ± 0.019
Altitude begin (km)	~70 km	Eccentricity	0.410 ± 0.013
Latitude end (°, N)	35.557 ± 0.014	Inclination (°, J2000)	4.228 ± 0.070
Longitude end (°, W)	120.487 ± 0.080	Argument of perihelion (°)	79.20 ± 0.13
Altitude end (km)	21.0 ± 0.5	Node (°)	30.458 ± 0.006
Altitude maximum (km)	29.5 ± 0.5	True anomaly (°)	280.49 ± 0.11
Azimuth radiant (S, °)	314.5 ± 0.8	Epoch (UT)	2015-10-24.24148
Entry angle (°)	50.6 ± 0.8	Mass (kg)	10–100
Convergence angle (°)	7.2 ± 0.2	Diameter (m)	0.20–0.40
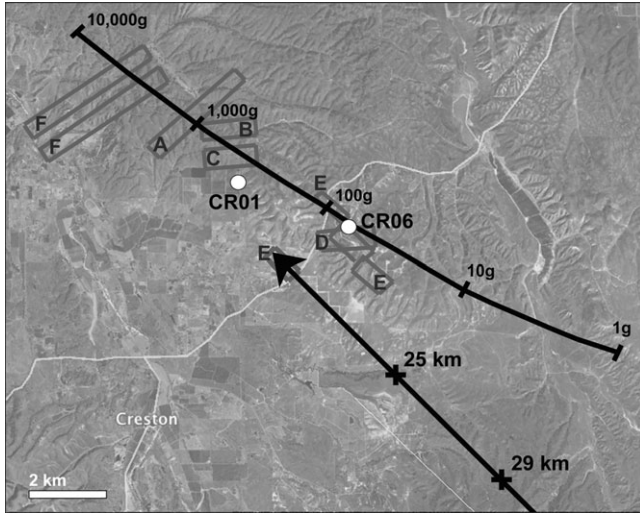
Fig. 5. Creston meteorite strewn field map (inset to Fig. 2). The ground-projected meteor trajectory (arrow) has 25 and 29 km altitude points marked. The calculated fall locations for meteorites of different masses (1 g–10 kg) are shown by a tick line. Radar reflections from falling meteorites are labeled (A–F). White dots show the actual find location of meteorites.

Fig. 6. Error range in the derived semimajor axis and inclination for local and global astrometry of the DFN allsky image.

camera observations. The (1-sigma) uncertainty in the triangulation was evaluated by a Monte Carlo simulation around the three velocity components. Two calibration methods were taken to derive the astrometry from the DFN camera, which resulted in slightly different positions of the trajectory. The first used star positions localized in the region around the meteor trajectory to fit the lens distortion parameters. The second used a global calibration. The localized method resulted in less systematic errors, but higher random errors as fewer stars were involved. The global effort may seem more accurate, but appeared to introduce systematic errors at the position of the meteor. This is clearly shown in Fig. 6, which gives two orbital elements of the fitted pre-atmospheric orbit for a range of solutions that cover the astrometric uncertainty. The calculated trajectory shifted by 2.3 km SE in the global method compared to the local method. The resulting direction of the radiant was different by 0.8°, which translates into a 0.3° systematic error in inclination. On the other hand, because of the large distance to the meteor, the velocities are not much affected. By comparing the measured trajectory positions to that of the recovered meteorites (Fig. 5), we were able to determine that the local calibration method gave the most reliable results. Those are tabulated in Table 3.

Using the wind sonde data from Oakland at 0 h and 12 h UT (http://weather.uwyo.edu/upperair/sounding.html), the wind drift of meteorites of different masses were calculated assuming a spherical shape and density of 3.2 g cm^{-3}. Figure 5 shows the calculated
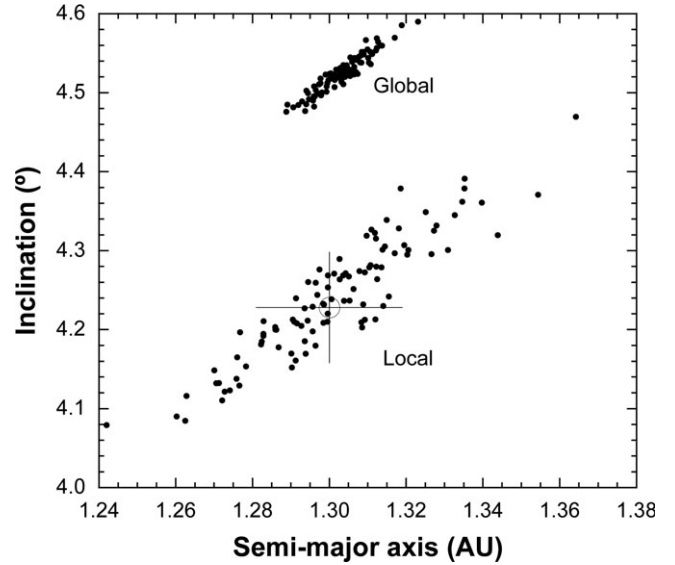
positions relative to the first-method trajectory for 1 g, 10 g, 100 g, and 1 kg masses falling from an altitude of 29 and 25 km, at the time of the flares. Notice how the recovered meteorite masses were found close to the predicted positions for the trajectory calculated using the local calibration method.

Six Doppler radar returns from three separate radars of the NOAA NEXRAD weather radar network were identified that could be from falling meteorites or dust (Bouvier et al. 2017). The earliest radar signature ("A," Fig. 5) appears in imagery from the radar with call letters "KVTX" (Los Angeles, California, with location shown in Fig. 2) at an altitude of 16.5 km above sea level (ASL) at 05:49:10.4 UTC—just 80 s after the meteor passed the 29.5 km altitude point (05:47:50.3 UTC), where the first breakup was recorded as a flare in the meteor imaging (Fig. 1). The radar-reported timing (05:47:57.6 UTC) is corrected for the time it takes the radar to adjust to the next-higher elevation level with each sweep. The new time implies that this signature "A" is due to fine material, approximately ~0.06 g in mass. However, it is found above the 1.2 kg point in the predicted strewn field.

Radar "KVBX" (Vandenberg Air Force Base) recorded signatures of what may be falling meteorites from 5.8 km ASL at 05:50:06.5 UTC ("B" and "C," Fig. 5), and from 6.9 km ASL at 05:51:36.3 UTC ("D"). The time lag of 136 s and 225 s to those altitudes, respectively, would correspond approximately to the fall time of 68 g and 3.5 g meteorites. Instead, these signatures are found above the 700 g and 70 g

points, respectively (Fig. 5). Radar "KHNX" (San Joaquin) recorded several returns at 05:51:34.1 at an altitude of 4.0 km, from 14 g meteorites ("E," Fig. 5). These reflections are above the 90 g point.

Finally, "KMUX" (San Francisco) recorded a pair of returns at 16.6 km altitude at 06:00:02.7 UTC ("F," Fig. 5), many minutes after the meteor. They are perhaps due to slow falling fine debris.

All recovered ~100 g meteorites are fully fusion crusted (Fig. 1), which confirms that they originated in a breakup before the end of the luminous trajectory. In contrast, the radar returns are only consistent with the measured trajectory if there was aggressive ongoing fragmentation after the main breakups at 29 and 25 km altitude. In particular, the final detection suggests ongoing fragmentation following the 29 km breakup and small debris settling to lower altitudes. Such ongoing fragmentation was also observed during breakup of the Novato meteoroid (Jenniskens et al. 2014). It is not impossible that these small 3–10 g meteorites would consist of broken fragments that are not fully crusted.

The light curve of this event is remarkably flat (Fig. 7). Each break in the DFN camera trace (marked "SV") provided a brightness measurement. The SkySentinel cameras ("RV" and "ES") brightness in each video frame was calibrated using the image of the Moon (Fig. 3), as well as the images of stars in the integrated image. Finally, the photographic trace is shown as a line marked "GO." Based on the CAMS video, the peak intensity of the very brief first (29 km) flare may be half a magnitude brighter, during a 1/60th second video field, than measured from the integrated intensity of the photometric trace (arrow).

The fall area is not far from the San Andreas Fault and densely populated by seismic stations. Seismic signatures were detected by nine stations (Table 4). Several traces show two bursts, possibly from the 29 and 25 km breakup events (Fig. 8). If so, the
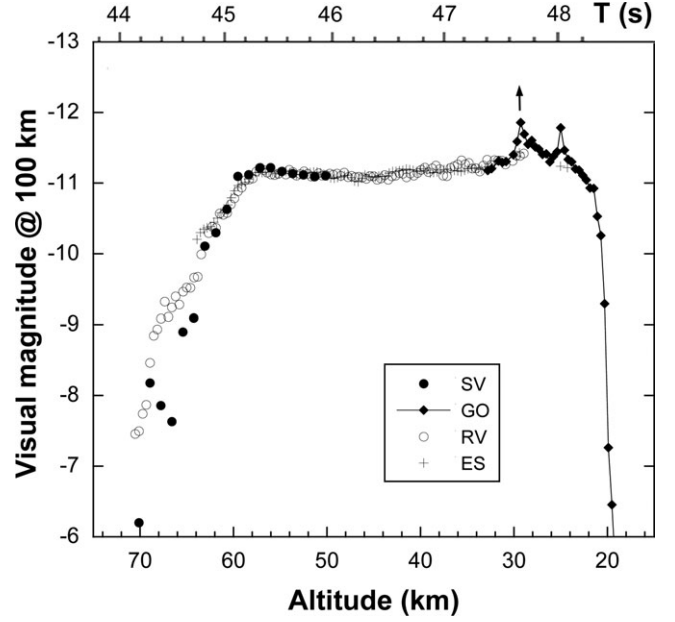

Fig. 7. The meteor visual light curve as seen from each camera station, normalized to a common distance of 100 km, as a function of time after 05:47:00 UTC and altitude.

corresponding distances imply a relatively high 334 m s^{-1} average sound speed. The strongest signal was measured at station SMM (Simmler) close to the track in the uprange direction, and that one is single-peaked, just like the signal at station MPP (Macpherson Peak) in about that same azimuthal direction. In this direction, the shock waves appear to have overlapped.

Mineralogical and Geochemical Properties of the Meteorite

The meteorite's interior was light gray and sprinkled with small (<1 mm) metal and troilte grains, as described by Bouvier et al. (2017). The stones exhibit shock melt veins, some to 2 mm thick, which are

Table 4. Seismic detections of the sonic boom.

Station ID	Station Name	Latitude (N)	Longitude (W)	Altitude (m)	Arrival Time (UT)	Relative Time (s)[a]	Range (km)[b]	Az (S, °)
CI.PHL	Park Hill	35.40773	120.54556	355	05:49:30.0	101.2	33	46
PB.B072	Parkfield	35.83100	120.34500	398	05:50:12.5	143.7	47	190
PB.B078	Parkfield	35.83770	120.34520	387	05:50:12.5	143.7	48	190
PB.B079	Parkfield	35.71570	120.20570	437	05:49:58.0	129.2	42	220
PB.B901	Parkfield	35.68970	120.14200	275	05:50:05.5	136.7	44	231
PB.B900	Parkfield	35.68600	120.00300	220	05:50:33.5	164.7	52	242
CI.VES	Vestal	35.84089	119.08469	154	05:54:25.0	396.2	130	256
CI.SMM	Simmler	35.31420	119.99581	599	05:50:41.5	172.7	53	299
CI.MPP	McPherson Peak	34.88848	119.81362	1739	05:52:19.0	270.2	93	321

[a]Time relative to 05:47:48.8 UT.
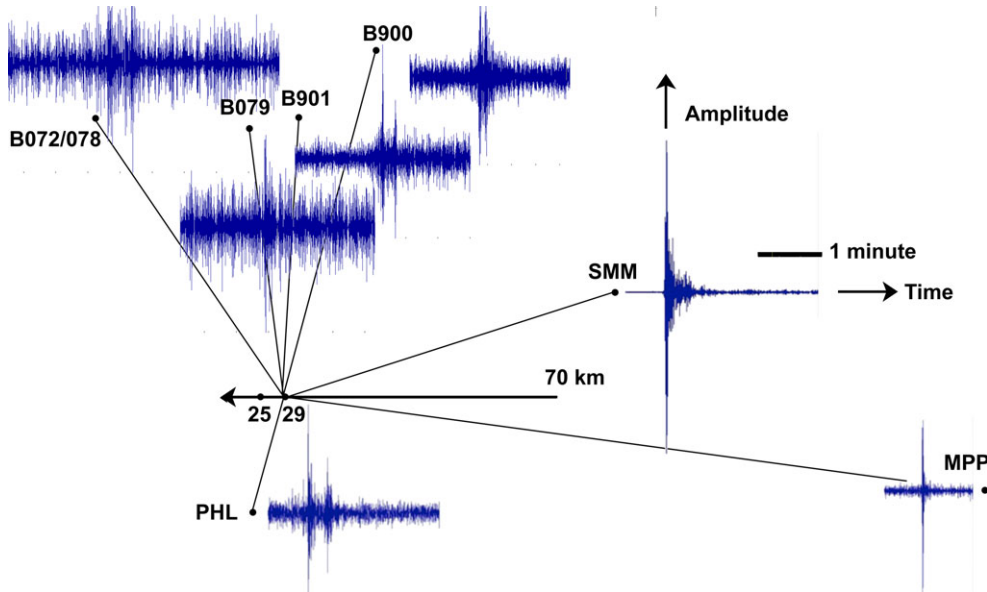[b]From 29.5 km altitude fragmentation event.

Fig. 8. Airburst generated seismic signatures as seen in different azimuth directions relative to the meteor trajectory (arrow).

sometimes broken at places along well-developed shiny black slickenside surfaces. We analyzed the moderately and highly shocked lithologies separately, for comparison. We found that olivine in both lithologies had identical compositions (and so are combined here), being an average olivine composition $Fa_{23.3\pm1.4}$ and a maximum CaO content of 0.053 (PMD=2.1%, $n = 10$), and low-Ca pyroxene with an average composition of $Fs_{23.5\pm3.5}Wo_{1.2\pm0.5}$ (PMD = 1.4%, $n = 8$), with Fe/Mn = 28.0 $\pm$ 2.2. These results differ slightly from those reported by Bouvier et al. (2017). These earlier results were: $Fa_{24.8\pm0.4}$ ($n = 11$), $Fs_{21.1\pm0.2}Wo_{1.3\pm0.2}$ ($n = 14$), with pyroxene Fe/Mn = 28.1 $\pm$ 1.3. Differences may be on account of varying equilibration of olivine and pyroxene grains or chondrules across the sampled stones.

Only two barred olivine chondrules were apparent in the investigated section. Plagioclase grains up to 200 μm are abundant, with compositions generally in the range $An_{26}Ab_{61}Or_{13}$ to $An_{27}Ab_{62}Or_{11}$, with one aberrant grain found with the composition $An_{18}Ab_{70}Or_{11}$. Chromite and troilite grains measuring up to 300 μm, and Fe-Ni metal grains up to 400 μm are abundant. As reported by Bouvier et al. (2017), a well-developed 1 mm thick shock vein had the typical blebs and spheres of Fe-Ni metal and sulfides. Fine-grained melt pockets were present but rare. Shock melt veins and pockets are heterogeneously distributed throughout the section, indicating a shock level of S4 (Stöffler et al. 1991).

The thin section may not be typical of all meteorites. X-ray CT scans of CR05 (Fig. 9, left) and CR06 (Fig. 9, right) were obtained by methods

described in Jenniskens et al. (2014), and show only sparse and thin shock veins, without clear interconnected irregular melt veins, which is more typical of shock stage S3 (Stöffler et al. 1991). Brecciation is evident from a nonhomogeneous distribution of metals and chondrules, the bright white spots and dark roundish features in Figs. 9C and 9D, respectively.

The new results appear to be slightly less equilibrated than L6, but are within the compositional field of L5/6, and therefore suggest rather more variable metamorphic heating than had been previously proposed. We classify the meteorite as L5/6 and shock stage S3/4, with weathering stage W0.

The classification of L is confirmed by the magnetic susceptibility $^{10}\log(\chi)$, measured at U.C. Davis. The value ranged from 4.79 to 4.93, with a mean of 4.86, which is in the middle of the range for unweathered L-type chondrites (Rochette et al. 2012). The measurement depended on the orientation of the meteorite in the magnetic susceptibility bridge. Trace element abundances compared to those of standard Orgueil (Table 5) also align better with the average of L chondrites than that of, say, LL chondrites (Fig. 10).

Further confirmation comes from oxygen and chromium isotope analysis of two independent aliquots of Creston. Stable isotope data results for CR01 in ‰ VSMOW are: $\delta^{17}O' = 3.537$, 3.781, and 3.618; $\delta^{18}O' = 4.582$, 5.210, and 4.828; and $\Delta^{17}O' = 1.118$, 1.030, and 1.069, respectively. The prime symbol refers to values of the ratio $^{17}O/^{16}O$ and $^{18}O/^{16}O$ being plotted on a natural log scale, so that dependencies are linear: $\delta^{17}O' = 1000 * \ln$
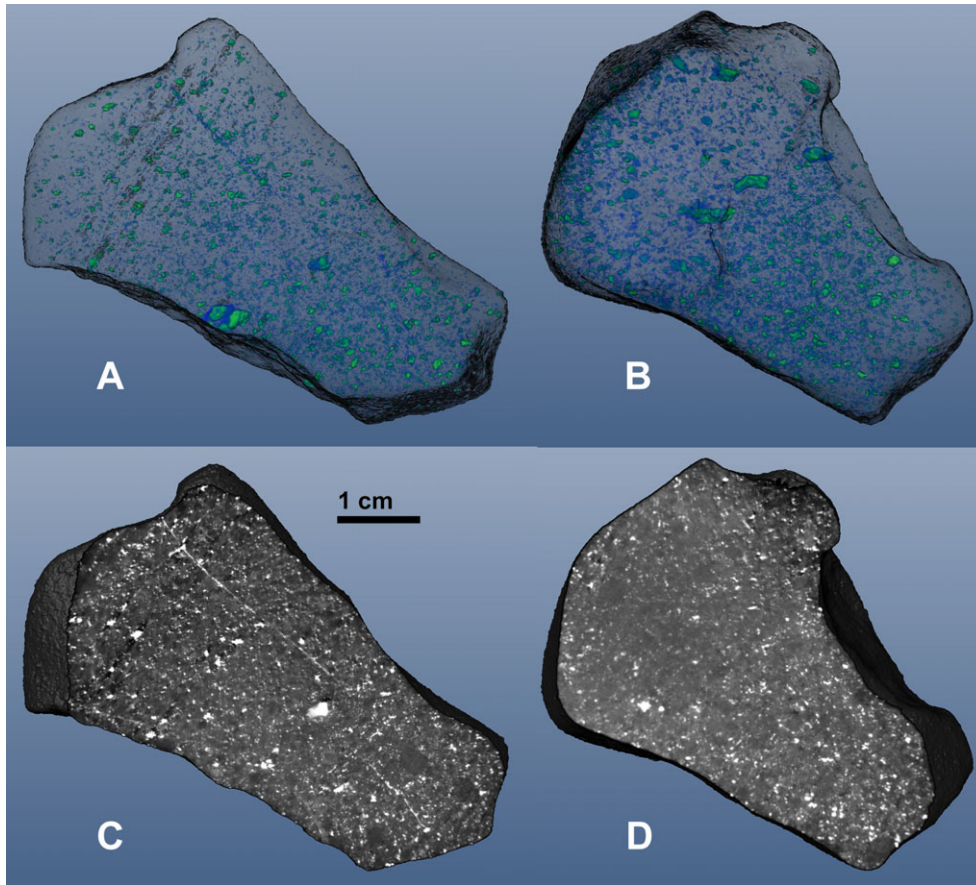
Fig. 9. X-ray CT scans of Creston meteorite CR05 (A and C) and CR06 (B and D). Top diagrams (A and B) visualize the 3-D internal metal grain distribution. Metal grains have highest density for X-rays. Bottom panels (C and D) show CT slices through the meteorites. The diffuse gray corresponds to the fine grain matrix, while the bright white spots correspond to the metal grains and metal-filled shock veins.

($[^{17}O/^{16}O]_{sample}/[^{17}O/^{16}O]_{standard(VSMOW)}$), and similar for $\delta^{18}O'$ (Jenniskens et al. 2012). These values fall within the range of other known L chondrites: $\delta^{17}O' = 3.0–3.8$ and $\delta^{18}O' = 4.2–5.6$, in the overlap area between L and LL and at the upper end of the $\delta^{17}O'$ range (Clayton et al. 1991). Combined with the olivine composition, the oxygen isotope values place Creston squarely in the L chondrite domain (Fig. 11). The $\epsilon^{54}Cr$ isotopic composition of Creston is -0.38 ± 0.11. This isotopic composition is indistinguishable from previously analyzed L chondrites including Knyahinya, Novato, Villalbeto de la Peña, and Lundsgård (Trinquier et al. 2007; Jenniskens et al. 2014; Schmitz et al. 2016). When combining $\epsilon^{54}Cr$ and $\Delta^{17}O$ isotopic compositions, Creston plots directly within the ordinary chondrite field (Fig. 11).

The crack distribution in X-ray CT scans implies a density of 0.5 fractures/cm^2 larger than 1 cm in length and a Weibull coefficient of $\alpha = 0.22 \pm 0.10$, which compares to the $\alpha = 0.185$ measured for L5, S3, Bluff (a) (Bryson and Ostrowski 2017). The bulk density of the meteorite determined with a helium pycnometer is 3.2933 ± 0.0005 g cm^{-3} (CR05) and 3.2486 ± 0.0006 g cm^{-3} (CR06), compared to 3.42 ± 0.05 g cm^{-3} for Villalbeto de la Peña (Llorca et al. 2005). The grain density is 3.597 ± 0.010 and 3.583 ± 0.004 g cm^{-3}, respectively (Villalbeto de la Peña: 3.59 ± 0.05 g cm^{-3}) for a porosity of 8.44 ± 0.02 and $9.33 \pm 0.01\%$ (Villalbeto: 4.7%), using methods described in Ostrowski and Bryson (2016).

Meteorite Collision History

Negligible activity of ^{60}Co (<1.7 dpm kg^{-1}) suggests that the pre-atmospheric size of the Creston meteoroid was rather small and no significant production of secondary thermal neutrons took place within the meteoroid during its recent cosmic ray exposure in space (Table 6). Normalized to the composition of an ordinary L chondrite, the measured ^{26}Al activity is consistent with that expected for a small-size L chondrite (Bhandari et al. 1989; Bonino et al. 2001; Leya and Masarik 2009).

Table 5. Major, minor, and trace element composition in Creston.

		Orgueil (this)	Orgueil[a]	Creston			Orgueil (this)	Orgueil[a]	Creston
Li	ppm	1.52	1.47	1.02	Cd	ppm	0.691	0.674	0.028
Be	ppm	0.022	0.03	0.028	Sb	ppm	0.14	0.13	0.057
Na	Wt%	0.49	0.5	0.63	Cs	ppb	0.187	0.189	0.008
Mg	Wt%	9.53	9.58	12.28	Ba	ppm	2.3	2.46	2.311
Al	Wt%	0.81	0.85	0.94	La	ppm	0.242	0.246	0.401
P	Wt%	0.11	0.1	0.15	Ce	ppm	0.63	0.6	0.898
K	Wt%	0.057	0.054	0.065	Pr	ppm	0.088	0.091	0.133
Ca	Wt%	0.88	0.92	1.19	Nd	ppm	0.478	0.464	0.628
Sc	ppm	5.85	5.9	7.43	Sm	ppm	0.149	0.152	0.199
Ti	Wt%	0.055	0.05	0.071	Eu	ppm	0.061	0.058	0.081
V	ppm	60.2	54.3	71.9	Gd	ppm	0.203	0.205	0.311
Cr	ppm	2705	2650	1903	Tb	ppm	0.042	0.038	0.055
Mn	Wt%	0.2	0.19	0.24	Dy	ppm	0.248	0.255	0.419
Co	ppm	510	506	320.9	Ho	ppm	0.59	0.057	0.083
Fe	Wt%	19.33	18.5	19.01	Er	ppm	0.159	0.163	0.25
Ni	Wt%	1.01	1.08	0.101	Tm	ppm	0.027	0.026	0.038
Cu	ppm	127	131	74.8	Yb	ppm	0.161	0.169	0.263
Zn	ppm	318	312	36.6	Lu	ppm	0.028	0.025	0.039
Ga	ppm	8.98	9.8	2.72	Hf	ppm	0.101	0.106	0.175
Rb	ppm	2.27	2.31	2.07	Ta	ppm	0.018	0.015	0.021
Sr	ppm	7.8	7.81	7.81	Tl	ppm	0.127	0.142	0.003
Y	ppm	1.6	1.53	1.89	Pb	ppm	2.61	2.63	0.051
Zr	ppm	3.9	3.62	5.11	Th	ppm	0.033	0.031	0.049
Nb	ppm	0.288	0.279	0.351	U	ppm	0.007	0.008	0.016

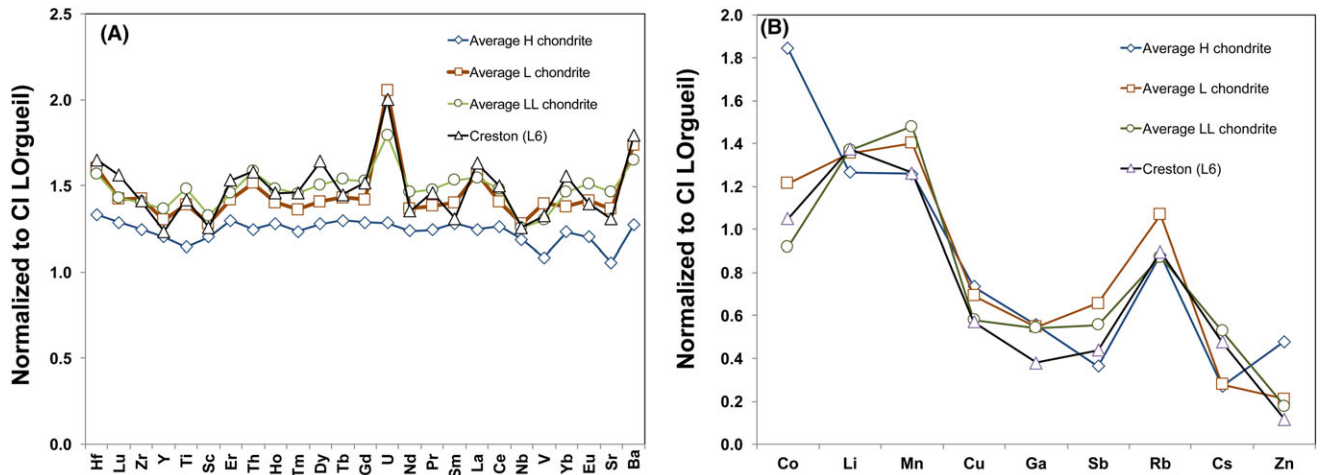[a]Reference values for Orgueil taken from Lodders (2003) and Lodders et al. (2009).

Fig. 10. Trace element abundances relative to Orgueil in order of decreasing condensation temperature for (A) refractory siderophile and lithophile elements and (B) for chalcophile elements and halogens.

When we compare the radionuclide concentrations with cosmic ray production estimations for ^{26}Al (Leya and Masarik 2009), ^{60}Co (Eberhardt et al. 1963; Spergel et al. 1986), ^{54}Mn (Kohman and Bender 1967), and ^{22}Na (Bhandari et al. 1993), the best agreement in the sequence of the given isotopes is obtained for radii of $r = 10–20$ cm, <20 cm, 8–12 cm, and 5–10 cm, respectively. These are upper limits to the size at the time of fall. Combining all results, we infer a roughly spherical meteoroid with 10–20 cm radius. The ^{22}Na/^{26}Al ratios of the two specimens are 1.42 ± 0.15 and 1.55 ± 0.17, respectively. That makes Creston similar to Jesenice with respect to the radionuclide content (Bischoff et al. 2011).
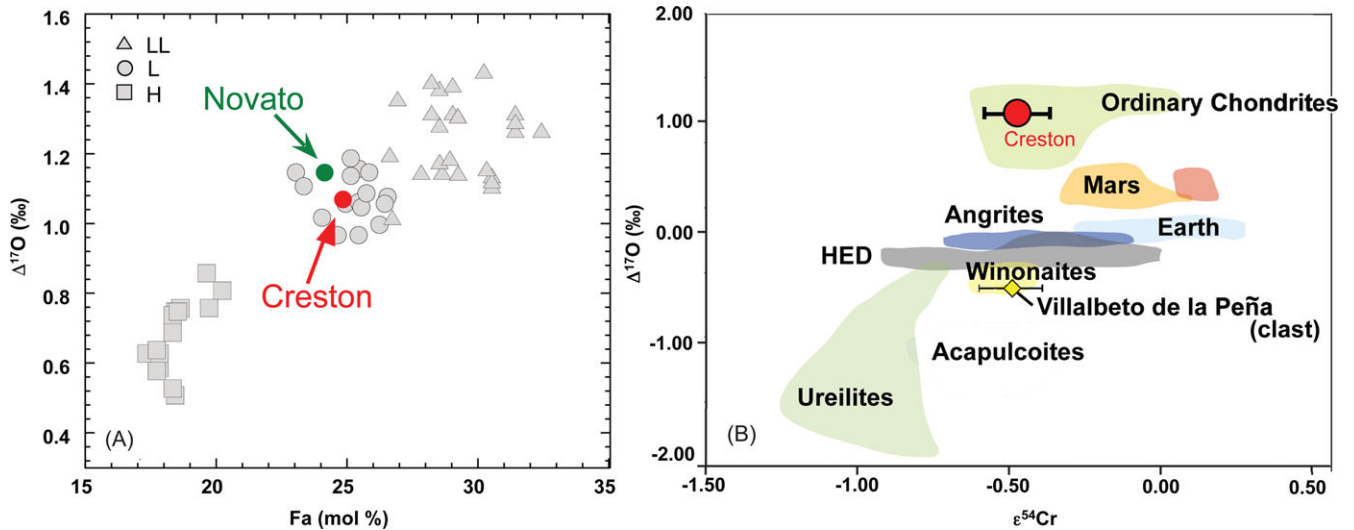
Fig. 11. Meteorite classification. A) $\Delta^{17}O$ versus Fa mol% in olivine in Creston compared with other ordinary chondrites, based on data from Troiano et al. (2011) and references therein, Popova et al. (2013), and Jenniskens et al. (2014). B) Comparison of the $\Delta^{17}O$-$\varepsilon^{54}Cr$ isotopic composition of Creston with achondrite and noncarbonaceous chondrite groups. Adapted after Schmitz et al. (2016), also plotting the Winonaite clast of Villalbeto de la Peña (Bischoff et al. 2013).

Table 6. Massic activities of cosmogenic radionuclides (in dpm kg^{-1}) corrected to the time of fall of the meteorite October 24, 2015. Errors in gamma-ray activities include a 1σ uncertainty of 10% in the detector efficiency calibration; those in AMS activities are dominated by counting statistics.

Nuclide Method	Half-life –	CR02 (dpm kg^{-1}) AMS	CR05 (dpm kg^{-1}) γ-ray	CR06 (dpm kg^{-1}) γ-ray
^{58}Co	70.83 d	–	9 ± 4	<14
^{56}Co	77.236 d	–	<18	8 ± 3
^{46}Sc	83.787 d	–	14 ± 3	<12
^{57}Co	271.8 d	–	6 ± 1	8 ± 1
^{54}Mn	312.3 d	–	58.0 ± 5.9	52.7 ± 5.4
^{22}Na	2.60 y	–	68.4 ± 5.0	72.6 ± 5.4
^{60}Co	5.27 y	–	<1.7	<1.7
^{44}Ti	60 y	–	<2.8	<2.7
^{36}Cl	3.01 × 10^5 y	8.6 ± 0.1	–	–
^{26}Al	7.17 × 10^5 y	–	48.2 ± 3.6	46.7 ± 3.7
^{10}Be	1.39 × 10^6 y	20.3 ± 0.2	–	–

The activity of the short-lived radioisotopes with half-life less than the orbital period represents the production integrated over the last segment of the orbit. The fall of Creston occurred during the solar cycle 24 maximum. The cosmic ray flux was low in the 6 months prior to the fall, so that the activities for the very short-lived radionuclides are expected to be low (see Table 6). The naturally occurring radionuclides (Table 7) are low also, but in the range of other concentrations measured in ordinary L chondrites (Wasson and Kallemeyn 1988).

Table 7. Concentration of primordial radionuclides (ng g^{-1} for U and Th chains and mg g^{-1} for ^{40}K) in the specimens of the Creston stone measured by nondestructive gamma-ray spectroscopy. Errors include a 1σ uncertainty of 10% in the detector efficiency calibration.

Nuclide	Half-life	CR05	CR06
^{232}Th	1.405 × 10^{10} y	35.5 ± 2.5	34.2 ± 2.4
^{238}U	4.468 × 10^9 y	9.8 ± 0.8	9.2 ± 0.8
^{40}K	1.251 × 10^9 y	810 ± 80	720 ± 70

The ^{10}Be concentration of 20.3 dpm kg^{-1} is consistent with irradiation near the center of an object with a radius of about 20 cm (Leya and Masarik 2009) or a near-surface irradiation (5–10 cm depth) in a larger object (up to ~75 cm radius). The ^{36}Cl concentration of 8.6 dpm kg^{-1} shows no neutron-capture contribution and therefore favors a relatively small meteoroid. Combining ^{10}Be with ^{21}Ne concentration (see below) gives a ^{21}Ne/^{10}Be cosmic ray exposure age of 50–54 Ma.

Creston does not contain solar wind or other trapped noble gases. Hence, it is not a regolith breccia. Indeed, only a few % of all L chondrites are. Based on ^{22}Ne/^{22}Ne = 1.10 ± 0.01 (Table 8) and the model calculations by Leya and Masarik (2009), it derives from a meteoroid with at least 20 cm radius, consistent with the one derived from radionuclides. Creston has a CRE age of about 40–50 Ma based on the empirically calibrated ^{22}Ne/^{21}Ne-^{21}Ne and ^{22}Ne/^{21}Ne-^{38}Ar methods (Dalcher et al. 2013).

Table 8. Noble gas concentrations of He, Ne, and Ar in Creston.

	CR01-NG-1[a]	CR01-NG-2[a]	Total[a]
^{3}He	n.m.	n.m.	n.m.
^{4}He	742(3)	711(2)	725(2)
^{20}Ne/^{22}Ne	0.838(7)	0.839(6)	0.838(5)
^{21}Ne/^{22}Ne	0.913(1)	0.902(2)	0.907(1)
^{20}Ne	12.7(1)	12.9(1)	12.8(1)
^{36}Ar/^{38}Ar	0.736(23)	0.755(19)	0.746(15)
^{40}Ar/^{36}Ar	3230(100)	3200(80)	3210(60)
^{36}Ar	1.76(6)	1.78(4)	1.77(4)
^{22}Ne$_{cos}$/^{21}Ne$_{cos}$	1.09(1)	1.11(1)	1.10(1)
^{21}Ne$_{cos}$	15.17(4)	15.40(4)	15.30(3)
^{38}Ar$_{cos}$	2.35(2)	2.30(2)	2.32(1)
^{4}He$_{rad\ (=non-cos)}$	336(31)	295(32)	314(31)
CRE-^{21}Ne (Ma)	39(5)	42(6)	41(6)
CRE-^{38}Ar (Ma)	50(2)	51(2)	50(2)
U,Th-He (Ga)	1.11	0.99	1.05
K-Ar (Ga)	4.32	4.31	4.31
Mass (mg)	32.6	37.0	69.6

[a]All concentrations are given in 10^{-8} cm³ STP/g (1 cm³ STP = 2.687×10^{19} atoms). Values in parentheses indicate uncertainties on the last digit. Uncertainties of concentrations (and thus, CRE ages) do not include the uncertainty of the standard amounts, which is about 3%. T = CRE ages, R = radiogenic gas retention ages.

The U,Th-He age (corrected for cosmogenic ^{4}He via ^{21}Ne$_{cos}$) of Creston is ~1 Ga and the K-Ar age is ~4.3 Ga (Table 8). Both are significantly higher than their counterparts in L chondrite Villalbeto de la Peña, which has a similar CRE age as Creston. Both ages assume L-chondritic abundances of K, U, and Th listed in Tables 4 and 7 (Wasson and Kallemeyn 1988).

The U-Pb systematics of Creston apatite reveals an upper intercept age of 4497.9 ± 5.8 Ma (Wetherial diagram) and 4496.7 ± 5.8 Ma (2σ) (Tera-Wasserburg diagram), respectively. Results for individual apatite grains are given in Table 9. A total of 37 apatite grains give a weighted average ^{207}Pb/^{206}Pb age at 4497.1 ± 3.7 Ma (2σ) (Fig. 12). Compared to the earliest solar system solids having formed 4,568.2 Ma ago (Bouvier and Wadhwa 2010), the measured age is 71.1 ± 3.7 Ma after the formation of the solar system. The measurements also show a lower intercept age at 755 ± 320 Ma (Tera-Wasserburg reserve Concordia) and 771 ± 320 Ma (Wetherial Concordia), respectively.

DISCUSSION

The L Chondrite Source Region

Table 10 provides a summary of the various age estimates and compares results to those obtained from other L5 and L6 chondrite falls for which atmospheric trajectories and pre-atmospheric orbits were derived. Columns are in order of increasing semimajor axis of the orbit.

Note that each past orbit sampled a different range of CRE age (Table 10), suggesting all L chondrites studied so far originated in different collision events (Jenniskens et al. 2014). Creston's CRE age and oxygen isotope compositions are similar to those of Villalbeto de la Peña (Llorca et al. 2005), but Villalbeto de la Peña has a significantly different olivine Fa and pyroxene Fs mineral composition. This meteorite is otherwise exceptional also because it has a Winonaite-related fragment in a hydrothermally metamorphosed polymict L-chondritic breccia (Bischoff and Schultz 2004; Bischoff et al. 2013), suggesting Villalbeto de la Peña came from a different source altogether (Fig. 11). We still may be looking at all different collision events.

Oxygen isotope values for Creston differ significantly from those of Park Forest (Simon et al. 2004). While Creston plots closer to a group of both high δ17O' and δ18O' values for L chondrites in Clayton et al. (1991), Park Forrest plots closer to a group of both low values. This may point to different source regions. Novato has similar oxygen isotopes, mineral composition, and shock stage. The known ranges of oxygen isotope and olivine and pyroxene composition values (e.g., Rubin 1990; Clayton et al. 1991) are reflected in those measured for the six L chondrites with known orbits.

The U-Pb age of Creston is within error identical to, but with better precision than, the 4472 ± 31 Ma measured for L6 chondrite Novato (Yin et al. 2014). This is due to the fact the U-Pb data points for the measured phosphates in Creston are concentrated near the upper intercept (Fig. 12), whereas the data points for Novato (greater Pb loss) are spread along the discordia (cf. fig. 5 in Yin et al. 2014). Thus, the upper intercept age of Creston is better defined than Novato, while the opposite is true for the lower intercept ages. The age of upper intercept is thought to signify the time of blocking temperature for Pb diffusion in phosphate minerals associated with extensive collisional impacts. This shows significant impacts occurred on the L chondrite parent body until about 70 Ma after formation of the first solids (4568 Ma ago). This epoch was earlier linked to the Earth–Moon-forming giant impact, suggesting that fragments from that event impacted the parent body in the asteroid belt at relatively high speed (Yin et al. 2014; Bottke et al. 2015). Most recently, Barboni et al. (2017) suggested the Moon impact event occurred earlier than >4.51 ± 0.01 Ga ago, i.e., before 57 Ma after formation of the first solids in the solar system, more in line with the earlier suggestion based on Hf-W ages of the Moon-

Table 9. SIMS U-Pb isotopic data of apatite from Creston. Spot positions are identified in Fig. 4.

Spot	U (ppm)	Th (ppm)	Th/U	^{204}Pb (cps)	^{204}Pb/^{206}Pb	f_{206} (%)	^{207}Pb^a/^{206}Pb^a	±1σ (%)	^{207}Pb^a/^{235}U	±1σ (%)	^{206}Pb^a/^{238}U	±1σ (%)	$t_{207/206}$ (Ma)	±1σ	$t_{207/235}$ (Ma)	±1σ	$t_{206/238}$ (Ma)	±1σ
1-1@1	5.0	7.4	1.48	n.d.	—	—	0.5989	0.63	81.9	2.9	0.992	2.83	4505	9	4485	30	4441	92
1-1@2	5.6	8.3	1.48	n.d.	—	—	0.5900	0.69	84.7	3.9	1.042	3.81	4484	10	4520	40	4601	126
1-2@1	5.2	7.4	1.43	0.051	0.0003	0.57	0.5890	0.76	82.5	2.7	1.015	2.54	4481	11	4493	27	4518	83
1-2@2	5.9	9.1	1.54	n.d.	—	—	0.5917	0.92	80.9	3.2	0.992	3.04	4488	13	4473	32	4441	98
1-3@1	5.1	7.3	1.43	0.019	0.0001	0.21	0.5897	0.82	87.1	3.3	1.071	3.24	4483	12	4547	34	4693	109
2-1@2	5.3	8.8	1.67	n.d.	—	—	0.6074	0.48	81.3	3.6	0.971	3.54	4526	7	4479	36	4375	113
2-1@3	6.2	9.6	1.54	0.034	0.0003	0.55	0.5957	1.18	75.8	4.0	0.923	3.87	4497	17	4408	41	4215	121
2-1@4	5.2	8.0	1.52	0.034	0.0002	0.37	0.5957	1.14	84.0	3.2	1.023	2.94	4498	17	4511	32	4542	97
2-2@1	6.3	10.6	1.68	0.034	0.0002	0.35	0.5937	0.63	80.0	2.8	0.977	2.71	4493	9	4462	28	4393	87
2-2@2	5.9	10.3	1.73	n.d.	—	—	0.5963	0.33	83.0	4.1	1.009	4.07	4499	5	4499	42	4498	133
2-2@3	5.7	9.3	1.64	n.d.	—	—	0.5965	0.95	80.3	3.5	0.977	3.42	4500	14	4466	36	4392	110
2-2@4	7.5	13.0	1.74	0.085	0.0007	1.40	0.5904	0.82	81.9	3.3	1.007	3.15	4484	12	4486	33	4490	103
2-3@1	6.3	9.8	1.55	n.d.	—	—	0.5907	0.52	71.1	3.5	0.873	3.47	4485	8	4344	36	4046	105
2-3@2	7.0	10.9	1.57	0.102	0.0009	1.63	0.5791	0.65	69.2	3.0	0.867	2.93	4456	10	4317	31	4023	88
3-1@1	5.8	8.4	1.47	0.038	0.0003	0.50	0.5884	1.21	77.7	3.2	0.958	2.98	4480	18	4433	33	4333	95
3-1@2	7.2	10.5	1.47	n.d.	—	—	0.5944	0.76	78.6	2.7	0.959	2.58	4494	11	4444	27	4335	82
3-1@3	7.6	11.2	1.47	0.019	0.0002	0.29	0.5922	0.50	77.1	3.0	0.945	3.00	4489	7	4426	31	4288	95
4-1@1	5.6	8.0	1.43	n.d.	—	—	0.5980	0.29	82.5	3.3	1.000	3.34	4503	4	4493	34	4469	108
4-1@2	6.0	9.3	1.55	n.d.	—	—	0.5970	0.58	84.4	2.7	1.026	2.65	4501	8	4516	28	4551	87
4-1@3	7.5	10.9	1.45	n.d.	—	—	0.5986	1.10	78.0	4.6	0.945	4.47	4505	16	4437	47	4289	142
4-1@4	6.5	10.0	1.53	0.034	0.0003	0.55	0.5838	0.88	77.1	3.5	0.958	3.34	4468	13	4425	35	4332	106
4-1@5	6.1	10.3	1.69	n.d.	—	—	0.5926	0.59	78.1	3.8	0.956	3.72	4490	9	4439	39	4326	118
4-1@6	5.8	8.8	1.53	n.d.	—	—	0.5848	1.04	80.0	4.2	0.992	4.02	4471	15	4462	43	4443	130
4-1@7	5.5	8.2	1.49	n.d.	—	—	0.5978	0.69	84.5	2.9	1.025	2.84	4503	10	4517	30	4549	93
5-1@1	5.4	8.7	1.60	0.034	0.0002	0.42	0.5974	0.62	83.0	2.9	1.007	2.83	4502	9	4499	29	4492	92
5-1@2	5.6	10.0	1.77	0.057	0.0004	0.77	0.5961	0.74	89.1	3.4	1.084	3.32	4499	11	4570	35	4734	112
6-1@1	5.4	8.6	1.60	n.d.	—	—	0.6074	0.59	86.2	2.8	1.029	2.75	4526	9	4536	29	4561	91
6-1@2	5.1	8.0	1.58	n.d.	—	—	0.5903	0.93	90.7	3.6	1.114	3.49	4484	14	4588	37	4826	120
6-1@3	5.0	7.6	1.53	n.d.	—	—	0.6004	0.67	85.1	4.3	1.028	4.28	4509	10	4524	44	4559	141
7-1@1	4.4	5.9	1.34	n.d.	—	—	0.5994	0.47	91.2	2.8	1.103	2.80	4507	7	4593	29	4793	95
7-1@2	4.8	6.9	1.44	0.051	0.0003	0.63	0.5788	0.91	84.2	3.1	1.056	2.97	4456	13	4514	32	4646	99
14-1@1	4.6	7.3	1.59	n.d.	—	—	0.5950	0.80	89.4	2.8	1.090	2.72	4496	12	4574	29	4753	92
14-1@2	4.8	7.8	1.63	n.d.	—	—	0.5933	0.91	87.9	3.2	1.075	3.07	4492	13	4557	33	4706	103
16-1@1	5.1	7.8	1.55	n.d.	—	—	0.6091	0.95	96.3	3.3	1.146	3.13	4530	14	4648	33	4924	109
16-1@2	5.6	8.6	1.54	n.d.	—	—	0.6026	0.88	88.7	3.3	1.067	3.20	4514	13	4565	34	4681	107
16-1@3	5.8	9.2	1.58	n.d.	—	—	0.6011	0.82	95.2	2.8	1.149	2.71	4511	12	4637	29	4931	94
17-3@1	7.4	11.5	1.54	0.034	0.0001	0.22	0.5969	0.97	97.5	8.7	1.185	8.69	4500	14	4661	92	5038	311

^{a}Radiogenic, using the modern terrestrial Pb as common lead compositions ^{206}Pb/^{204}Pb = 18.703 and ^{207}Pb/^{206}Pb = 0.836 (Stacey and Kramers 1975); n.d. = not detected.
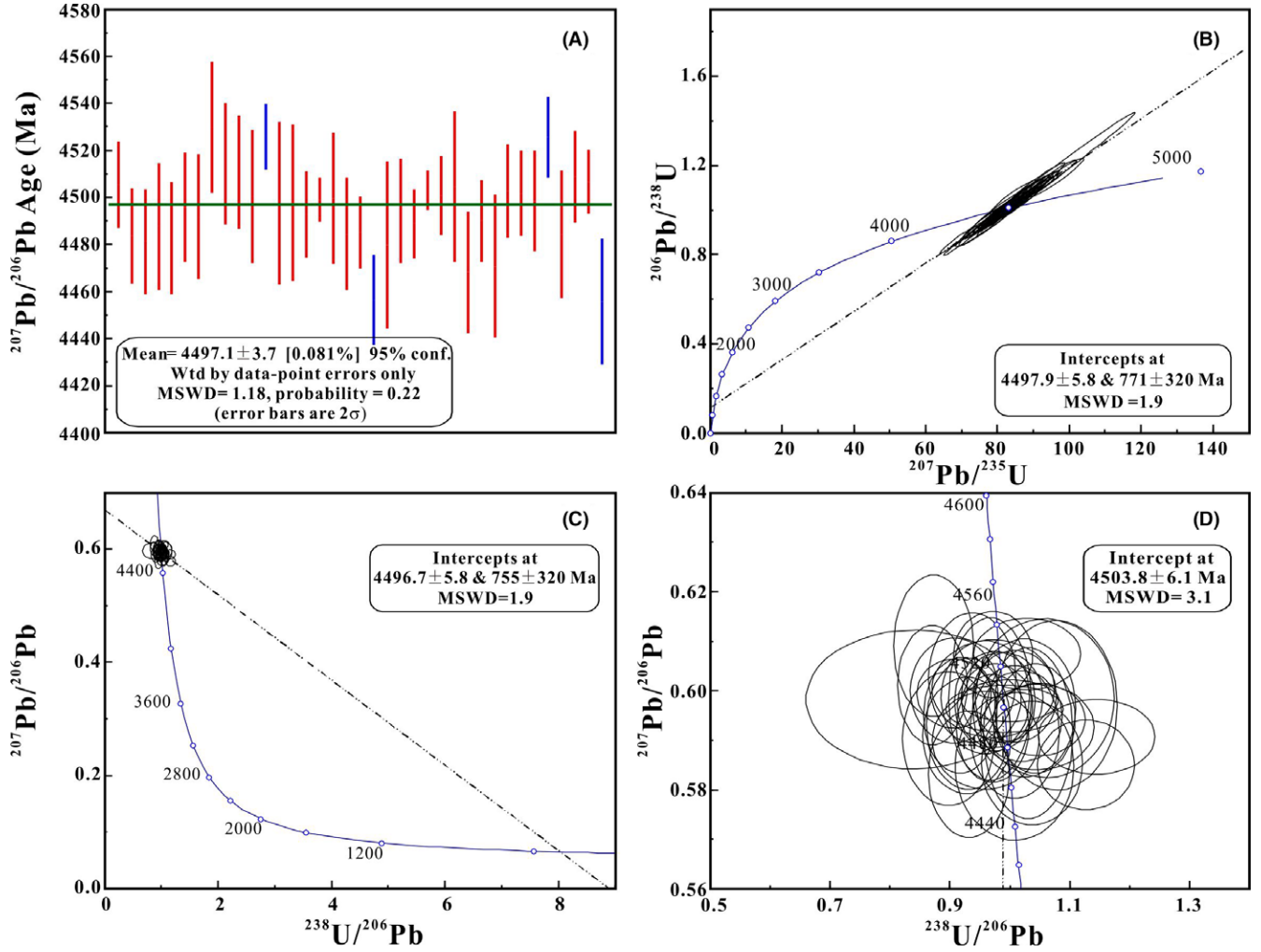
Fig. 12. Summary of Pb-Pb measurements on Creston. A) A mean Pb-Pb age is 4,497.1 ± 3.7 (0.081%), with 95% confidence. B) Intercepts for Pb-U age are at 771 ± 320 Ma and 4497.9 ± 5.8 [±11] Ma. MSWD = 1.9. C) Intercepts for Pb-Pb age are at 755 ± 320 Ma and 4496.7 ± 5.8 [±11] Ma. MSWD = 1.9. D) Detail of (C).

forming impact (e.g., Yin et al. 2014). The two interpretations of the Moon-forming giant impact timing are in apparent conflict, and require resolutions with future work.

Creston experienced additional heating events later in its history. The high K-Ar age and U,Th-He ages (Table 10) suggest that Creston's radiogenic clock was either not fully reset during the 467 Ma collision event that is thought to have formed the Gefion family, or that Creston originated from a source other than the Gefion family. The measured K-Ar age is identical to that of Innisfree (Goswami et al. 1978), an L5 (S3) type ordinary chondrite with a similar short semimajor axis orbit (Table 10). However, the lower intercept ages have such high uncertainty that they overlap with both the 1050 Ma U,Th-He age and the 467 Ma resetting signature detected in Novato (Jenniskens et al. 2014; Yin et al. 2014) and Park Forest (Meier et al. 2017).

The downward trend for U,Th-He ages relative to K-Ar ages is thought to be due to gas loss, with ^{4}He having a higher diffusivity than ^{40}Ar (and shorter half-life of ^{40}K relative to ^{238}U and ^{232}Th [Wasson 2012]). In the overall diagram of U,Th-He ages versus K-Ar ages (Fig. 13), Creston, Novato, and Park Forest are among the most displaced.

Solid gray symbols in Fig. 13 show meteorites for which U,Th-He, K-Ar and CRE ages are available. It is possible that Creston was liberated in the same collision as L5 Tane and L6 Nogata (Takaoka et al. 1989), L6 Mihonoseki (Shima et al. 1993), and L6 Kaptal-Aryk (Welten et al. 2001).

The orbit of Creston is considerably more evolved than that of previously observed meteorite falls. The semimajor axis is only 1.30 ± 0.02 AU, as opposed to 1.7–2.5 AU for other L chondrite falls observed so far. As with Villalbeto de la Peña, the cosmic ray exposure

Table 10. L chondrites with known orbits: classification criteria, collision history, and mean dynamical lifetimes for ejection from different source regions. The dynamical lifetimes in bold (1-sigma) and italic bold (2-sigma) are in agreement with the measured CRE age.

	Creston (this study)	Jesenice (1)	Innisfree (2)	Novato (3)	Villalbeto (4)	Park Forest (5)
Classification:	L5/6, S3/4	L6, S3	L5, S3 breccia	L6, S4 breccia	L6, S4 breccia	L5, S5 breccia
Fa	23.3 ± 1.4	25.1 ± 0.4	25.3 ± 0.2	24.1 ± 0.4	24.2 ± 0.2	24.7
Fs	23.3 ± 3.5	21.1 ± 0.4	–	20.7 ± 0.5	20.3 ± 0.2	20.7
Wo	1.2 ± 0.5	1.5	–	1.5 ± 0.2	1.6 ± 0.2	1.6
$\delta 17O'$	3.65 ± 0.12	–	–	3.70 ± 0.10	3.60 ± 0.26	3.44 ± 0.02
$\delta 18O'$	4.87 ± 0.32	–	–	4.83 ± 0.19	5.61 ± 0.50	4.68 ± 0.07
$\Delta 17O'$	1.072 ± 0.044	–	–	1.149 ± 0.022	1.1	–
K-Ar age (Ma)	4310 ± 100	3275 ± 205	4100 ± 300	550, 1520 ± 250	700	490 ± 70
^{40}Ar-^{39}Ar age (Ma)	–	~4300	–	–	–	–
U-Pb lower intercept age (Ma)	(755 ± 320)	–	–	473 ± 38	–	–
U,Th-He age (Ma)	1050 ± 60	2300 ± 500	–	460 ± 220	–	430 ± 90
U-Pb upper intercept age (Ma)	4496.7 ± 5.8	–	–	4472 ± 31	–	–
CRE age (Ma)	45 ± 5	~15	28 ± 3	9 ± 1[a]	48 ± 5	14 ± 2
Collisional lifetime in Main Belt (Ma)[b]	8.9	6.3	4.3	5.9	8.9	12.9
Semimajor axis (AU)	1.30 ± 0.02	1.75 ± 0.07	1.872	2.09 ± 0.08	2.3 ± 0.2	2.53 ± 0.19
Inclination (°)	4.23 ± 0.07	9.6 ± 0.5	12.28	5.51 ± 0.04	0.0 ± 0.2	3.2 ± 0.3
Dynamical age for ejection from inner belt:						
Hungaria (i ~ 23°)	–[c]	52.4 ± 1.8	58.1 ± 2.2	19.8 ± 3.2	31.6 ± 3.9	29.9 ± 2.4
ν_6 inner (a < 2.5; i < 4°)	22.2 ± 5.1	**12.2 ± 1.0**	**20.2 ± 2.3**	**9.4 ± 1.0**	11.9 ± 2.5	**13.7 ± 1.3**
ν_6 inner (a < 2.5; i > 4°)	**33.4 ± 11.0**	**11.3 ± 0.8**	11.2 ± 1.0	6.1 ± 0.4	13.8 ± 1.6	**12.2 ± 0.7**
4:1	9.2 ± 2.6	5.1 ± 0.6	12.9 ± 2.2	0.9 ± 0.7	2.5 ± 0.3	3.8 ± 0.4
7:2 (a < 2.5 AU)	21.3 ± 5.9	21.5 ± 2.3	18.9 ± 2.1	*28.1 ± 8.9*	15.3 ± 1.2	**16.3 ± 0.6**
3:1 (a < 2.5 AU)	12.9 ± 3.4	7.0 ± 1.1	11.1 ± 2.6	3.5 ± 1.8	1.2 ± 0.1	0.9 ± 0.2
From central belt:						
ν_6 inner (a > 2.5 AU)	–	**27.8 ± 22.8**	–	**15.8 ± 14.8**	~1.8	4.5 ± 2.0
7:2 (a > 2.5 AU)	–	**19.5 ± 5.8**	5.0 ± 2.4	**9.4 ± 5.1**	7.1 ± 3.9	**14.9 ± 4.6**
n6 outer (i ≤ 18°)	–	*7.1 ± 3.0*	8.7 ± 1.1	–	4.4 ± 1.4	6.8 ± 1.2
3:1 (a > 2.5, i > 6°, incl. Gefion family)	–	*48.1 ± 39.2*	21.1 ± 16.8	2.0 ± 0.6	6.8 ± 3.5	1.8 ± 0.4
3:1 (a > 2.5 AU, i < 6°)	10.4 ± 8.3	**11.1 ± 5.9**	*13.9 ± 7.3*	2.7 ± 0.9	0.8 ± 0.2	0.7 ± 0.1
ν_6 outer (i > 18°)	–	~24.4	13.7 ± 4.2	–	–	4.2 ± 1.5
Phocaea (i ~ 22°)	–	83.2 ± 14.6	78.6 ± 12.7	36.9 ± 15.8	**82.8 ± 38.2**	37.2 ± 8.2
Teutonia	4.9 ± 1.0	7.5 ± 1.3	12.0 ± 2.4	3.7 ± 0.4	1.3 ± 0.1	0.7 ± 0.1
8:3	–	**17.7 ± 7.3**	*12.5 ± 6.4*	0.9 ± 0.5	1.0 ± 0.3	2.4 ± 0.7
5:2 (incl. Gefion)	–	*7.3 ± 3.4*	*9.3 ± 7.7*	**6.3 ± 3.7**	0.5 ± 0.1	0.4 ± 0.1
From outer belt:						
2:1	–	*~10.7*	~10.6	–	–	0.7 ± 0.5

[a]With one collision in last 3–5 Ma.

[b]Collisional lifetime is based on size and is about 1.4 $\sqrt{r}$, with r the radius in cm. In Main Belt, based only on size: possibly underestimated by factor of 3–5 (see text).

[c]No model orbits evolved into a Creston-like orbit. Data from: (1) Bischoff et al. (2011), Welten et al. (2016); (2) Halliday (1977), Goswami et al. (1978), Rubin (1990); (3) Jenniskens et al. (2014); Yin et al. (2014); (4) Bischoff et al. (2013), Llorca et al. (2005); (5) Simon et al. (2004), and Meier et al. (2017).

age is considerably longer than the expected dynamical lifetime of ~9 Ma against collisions in the asteroid belt. The CRE age is inconsistent with the short dynamical lifetime of asteroids originating in the Gefion family (Jenniskens et al. 2014). Only highly inclined source regions or sources at the inner edge of the inner asteroid belt produce such long dynamical lifetimes.

Based on the measured orbit of Creston, the dynamical lifetimes were calculated for a range of possible source regions (Table 10). A model describing the evolution of small asteroids was
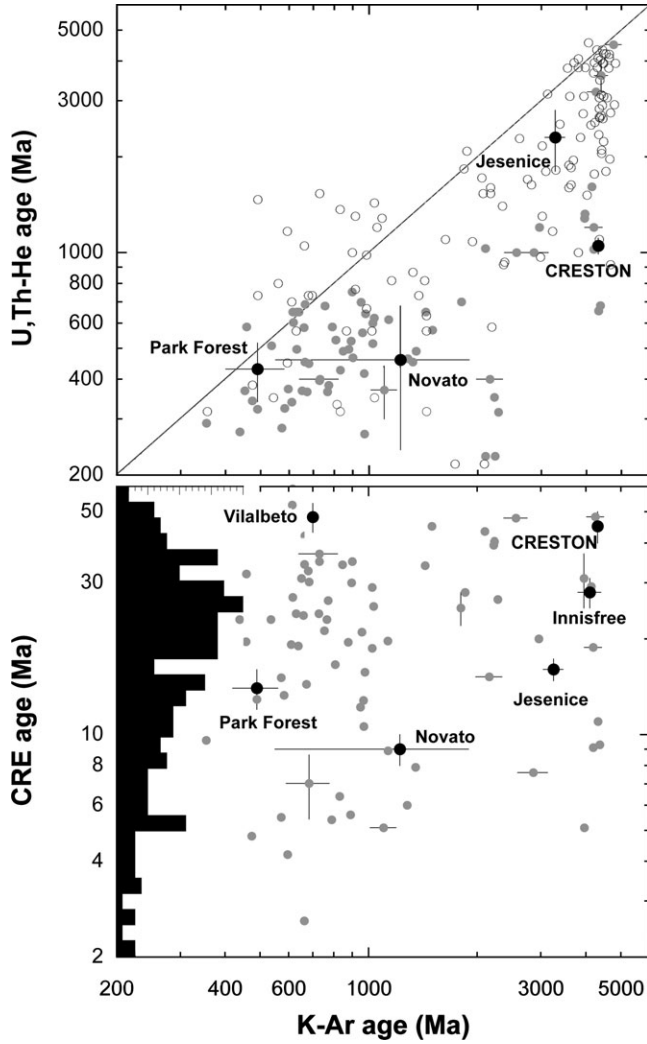
Fig. 13. U,Th-He and CRE age versus K-Ar age for L
chondrites. Solid circles are data from Crabb and Schultz
(1981), Takaoka et al. (1989), Marti and Graf (1992), Welten
et al. (2001, 2004), Eugster et al. (2007), Kita et al. (2013),
Trigo-Rodriquez et al. (2014), Leya (2015), Mahajan et al.
(2016), and Li et al. (2016). Open circles are U,Th-He and K-
Ar age data from Wasson (2012), for which no CRE age
information is available. Inset shows CRE histogram (range
$N = 0$–20) from Marti and Graf (1992) and more recent data,
including data with no K-Ar ages available.

developed that started with 92,449 test asteroids,
distributed across the Main Belt (Granvik et al. 2016,
2017). Of these, 70,708 evolved into NEO orbits.
Typically thousands of test asteroids originated from
each of several source regions. The median lifetime
was calculated and is listed in Table 10. The most
consistent source for Creston would be in the inner
asteroid belt at inclinations above 4°, arriving to
Earth via the ν_6 resonance. All other source regions
probed tend to produce shorter CRE ages or no
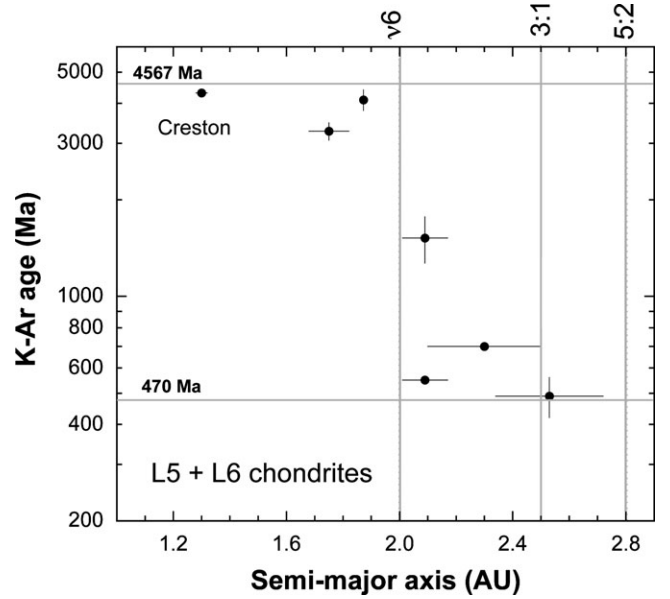model orbits evolved into a Creston-like orbit.

Fig. 14. The meteorite's K-Ar age compared to the semimajor
axis (a) of the impact orbit, showing that all meteorites with
high K-Ar ages impacted Earth on a short a <2 AU orbit.

The three meteorites with high K-Ar ages, Jesenice,
Innisfree, and Creston, are also the meteorites that
approached on short semimajor axis (a <2 AU) orbits
(Fig. 14). This would be consistent in a scenario where
these meteorites come to Earth via the ν_6 resonance
from a newly identified source region in the inner Main
Belt, but from three different collision events. The CRE
age of Jesenice is uncertain. The nominal 3.8 ± 0.3 Ma
CRE age may be underestimated, with signs of prior
exposure for ~15 Ma in a larger object prior to
breaking gently (i.e., perhaps not a collision) 1.6 Ma
ago (Welten et al. 2016). The ~15 Ma age would
correspond better to the 12 Ma dynamical lifetime
expected for a source deep in the inner asteroid belt,
arriving via the ν_6 resonance (Table 10).

The three meteorites have inclinations of 9.6°, 12.3°,
and 4.2°, suggesting that source has a ~4–13°
inclination. Candidate S-class asteroid families include
the small families associated with 254 Augusta
($a_{proper} = 2.19$ AU, $i_{proper} = 5°$) and 12 km 1646
Rosseland ($a_{proper} = 2.36$ AU, $i_{proper} = 8°$), and the large
family associated with 2076 Levin ($a_{proper} = 2.27$ AU,
$i_{proper} = 5°$), which has a formation age 366 ± 125 Ma
(Spoto et al. 2015). The Flora family was earlier
proposed as an L chondrite parent (Nesvorný et al.
2002), but is now thought to be the source of LL
chondrites (Popova et al. 2013; Jenniskens 2014).

The L chondrites with the 470 Ma signature have low
0–6° inclinations, lower than the 8.6–9.6° proper
inclination of the Gefion family. It is possible that another

source than Gefion is responsible for the shock-blackened L chondrites with the 470 Ma signature.

CONCLUSIONS

Creston and Novato originated from sites on the same L chondrite parent body that experienced one or more of the first hits after the Moon-forming event. Compositionally they are identical. However, CRE age and approach orbit on impact are different. While Novato arrived from a collision 9 Ma ago on an orbit that might be consistent with a collision cascade from the Gefion family and arriving at Earth via the 3:1 resonance, Creston's short impact orbit and high 45 ± 5 Ma CRE age imply it originated from the inner asteroid belt and came to Earth via the ν_6 resonance.

We postulate that the parent body of L chondrites was disrupted during the impact event recorded in U-Pb and Pb-Pb ages 4497 ± 6 Ma ago, after which two or more reassembled rubble pile daughter asteroids dispersed over the asteroid belt. The daughter asteroid of Novato may have settled in the middle asteroid belt and disrupted ~470 Ma ago. The daughter asteroid from which Creston originated ended up in the inner asteroid belt, not far from the ν_6 resonance.

The L chondrites with small semimajor axis orbits (a <2 AU), namely Creston, Innisfree, and Jesenice, sample three different collision events, perhaps from this same inner belt source. All three have a K-Ar age >3 Ga and are not shock-blackened.

Editorial Handling—Dr. Josep M. Trigo-Rodríguez

REFERENCES

Alexeev V. A. 1998. Parent bodies of L and H chondrites: Times of catastrophic events. *Meteoritics & Planetary Science* 33:145–152.

Anders E. 1964. Origin, age, and composition of meteorites. *Space Science Reviews* 3:583–714.

Arpesella C. 1996. A low background counting facility at Laboratori Nazionali del Gran Sasso. *Applied Radiation and Isotopes* 47:991–996.

Barboni M., Boehnke P., Keller B., Kohl I. E., Schoene B., Young E. D., and McKeegan K. D. 2017. Early formation of the Moon 4.51 billion years ago. *Science Advances* 3: e1602365.

Bhandari N., Bonino G., Callegari E., Cini Castagnoli G., Mathew K. J., Padia J. T., and Queirazza G. 1989. The Torino H6 meteorite shower. *Meteoritics* 24:29–34.

Bhandari N., Mathew K. J., Rao M. N., Herpers U., Bremer K., Vogt S., Wölfli W., Hofmann H. J., Michel R., Bodemann R., and Lange H.-J. 1993. Depth and size dependence of cosmogenic nuclide production rates in stony meteoroids. *Geochimica et Cosmochimica Acta* 57:2361–2375.

Bischoff A. and Schultz L. 2004. Abundance and meaning of regolith breccias among meteorites (abstract #5118). 67th Annual Meeting of the Meteoritical Society.

Bischoff A., Jersek M., Grau T., Mirtic B., Ott U., Kucera J., Horstmann M., Laubenstein M., Herrmann S., Randa Z., Weber M., and Heusser G. 2011. Jesenice—A new meteorite fall from Slovenia. *Meteoritics & Planetary Science* 46:793–804.

Bischoff A., Dyl K., Horstmann M., Ziegler K., and Young E. 2013. Reclassification of Villalbeto de la Peña— Occurrence of a Winonaite-related fragment in a hydrothermally metamorphosed polymict L-chondritic breccia. *Meteoritics & Planetary Science* 48:628–640.

Bonino G., Bhandari N., Murty S. V. S., Mahajan R. R., Suthar K. M., Shukla A. D., Shukla P. N., Cini Castagnoli G., and Taricco C. 2001. Solar and galactic cosmic ray records of the Fermo (H) chondrite regolith breccia. *Meteoritics & Planetary Science* 36:831–839.

Borovicka J., Spurny P., and Keclikova J. 1995. A new positional astrometric method for all-sky cameras. *Astronomy & Astrophysics Supplement* 112:173–178.

Bottke W. F., Durda D. D., Nesvorny D., Jedicke R., Morbidelli A., Vokrouhlicky D., and Levison H. F. 2005. Linking the collisional history of the main asteroid belt to its dynamical excitation and depletion. *Icarus* 179:63–94.

Bottke W. F., Vokrouhlicky D., Marchi S., Swindle T., Scott E. R. D., Weirich J. R., and Levison H. 2015. Dating the Moon-forming impact event with asteroidal meteorites. *Science* 348:321–323.

Bouvier A. and Wadhwa M. 2010. The age of the solar system redefined by the oldest Pb-Pb age of a meteoritic inclusion. *Nature Geoscience* 3:637–641.

Bouvier A., Gattacceca J., Agee C., Grossman J., and Metzler K. 2017. The Meteoritical Bulletin, No. 104. *Meteoritics & Planetary Science* 52. https://doi.org/10.1111/maps.12930.

Bryson K. L. and Ostrowski D. R. 2017. Meteorite fractures and scaling for asteroid atmospheric entry (abstract #2501). 48th Lunar and Planetary Science Conference. CD-ROM.

Clayton R. N., Mayeda T. K., Olsen E. J., and Goswami J. N. 1991. Oxygen isotope studies of ordinary chondrites. *Geochimica et Cosmochimica Acta* 55:2317–2337.

Crabb J. and Schultz L. 1981. Cosmic-ray exposure ages of the ordinary chondrites and their significance for parent body stratigraphy. *Geochimica et Cosmochimica Acta* 45:2151–2160.

Dalcher N., Caffee M. W., Nishiizumi K., Welten K. C., Vogel N., Wieler R., and Leya I. 2013. Calibration of cosmogenic noble gas production in ordinary chondrites based on ^{36}Cl- ^{36}Ar Ages. Part 1: Refined produced rates for cosmogenic ^{21} Ne and ^{38} Ar. *Meteoritics & Planetary Science* 48:1841–1862.

Eberhardt P., Geiss J., and Lutz H. 1963. Neutrons in meteorites. In *Earth science and meteoritics*, edited by Geiss J. and Goldberg E. D. Amsterdam, the Netherlands: North Holland. pp. 143–168.

Eugster O., Herzog G. F., Marti K., and Caffee M. W. 2006. Irradiation records, cosmic-ray exposure ages, and transfer times of meteorites. In *Meteorites and the early solar system II*, edited by Lauretta D. S. and McSween H. Y. Jr. Tucson, Arizona: The University of Arizona Press. pp. 829–851.

Eugster O., Lorenzetti S., Krähenbühl U., and Marti K. 2007. Comparison of cosmic-ray exposure age and trapped noble gases in chondrule and matrix samples of ordinary, enstatite, and carbonaceous chondrites. *Meteoritics & Planetary Science* 42:1351–1371.

Fieber-Beyer S. K. and Gaffey M. J. 2015. Near-infrared spectroscopy of 3:1 Kirkwood Gap asteroids III. *Icarus* 257:113–125.

Fries M., Fries J., Hankey M., and Matson R. 2016. Meteorite falls observed in U.S. Weather radar data in 2015 and 2016 (to date). 79th Meteoritical Society meeting, Berlin, Germany. Abstract. 1 p.

Goswami J. N., Lal D., Rao M. N., Sinha N., and Venkatesan T. R. 1978. Particle track and rare gas studies of Innisfree meteorite. *Meteoritics* 13:481–484.

Granvik M., Morbidelli A., Jedicke R., Bolin B., Bottke W. F., Beshore E., Vokrouhlicky D., Delbo M., and Michel P. 2016. Super-catastrophic disruption of asteroids at small perihelion distances. *Nature* 530:303–305.

Granvik M., Morbidelli A., Vokrouhlicky D., Bottke W. F., Nesvorny D., and Jedicke R. 2017. Escape of asteroids from the main belt. *Astronomy & Astrophysics* 598:A52.

Haack H., Farinella P., Scott E. R. D., and Keil K. 1996. Meteoritic, asteroidal, and theoretical constraints on the 500 Ma disruption of the L chondrite parent body. *Icarus* 119:182–191.

Halliday I. 1977. Photographic observations and orbit of the Innisfree meteorite. *Meteoritics & Planetary Science* 12:248–249.

Jenniskens P. 2014. Recent documented meteorite falls, a review of meteorite—Asteroid links. In *Meteoroids 2013*, edited by Jopek T., Rietmeijer F. J. M., Watanabe J., and Williams I. P. Proceedings of the astronomical conference held at A.M. University, Poznan, Poland, Aug 26–30, 2013. Poznan: A. M. University Press. pp. 57–68.

Jenniskens P., Gural P. S., Dynneson L., Grigsby B. J., Newman K. E., Borden M., Koop M., and Holman D. 2011. CAMS: Cameras for Allsky Meteor Surveillance to establish minor meteor showers. *Icarus* 216:40–61.

Jenniskens P., Fries M. C., Yin Q.-Z., Zolensky M., Krot A. N., Sandford S. A., Sears D., Beauford R., Ebel D. S., Friedrich J. M., Nagashima K., Wimpenny J., Yamakawa A., Nishiizumi K., Hamajima Y., Caffee M. W., Welten K. C., Laubenstein M., Davis A. M., Simon S. B., Heck P. R., Young E. D., Kohl I. E., Thiemens M. H., Nunn M. H., Mikouchi T., Hagiya K., Ohsumi K., Cahill T. A., Lawton J. A., Barnes D., Steele A., Burton A. S., Dworkin J. P., Elsila J. E., Pizzarello S., Ogliore R.,

Smitt-Kopplin P., Harir M., Hertkorn N., Verchovsky A., Grady M., Nagao K., Okazaki R., Takechi H., Hiroi T., Smith K., Silber E. A., Brown P. G., Albers J., Klotz D., Hankey M., Matson R., Fries J. A., Walker R. J., Puchtel I., Lee C. A., Erdman M. E., Eppich G. R., Roeske S., Gabelica Z., Lerche M., Nuevo M., Girten B., and Worden S. P. (the Sutter's Mill Meteorite Consortium). 2012. Radar-enabled recovery of the Sutter's Mill Meteorite, a carbonaceous chondrite regolith breccia. *Science* 338:1583–1587.

Jenniskens P., Rubin A. E., Yin Q.–Z., Sears D. W. G., Sandford S. A., Zolensky M. E., Krot A. N., Blair L., Kane D., Utas J., Verish R., Friedrich J. M., Wimpenny J., Eppich G. R., Ziegler K., Verosub K. L., Rowland D. J., Albers J., Gural P. S., Grigsby B., Fries M. D., Matson R., Johnston M., Silber E., Brown P., Yamakawa A., Sanborn M. E., Laubenstein M., Welten K. C., Nishiizumi K., Meier M. M. M., Busemann H., Clay P., Caffee M. W., Schmitt–Kopplin P., Hertkorn N., Glavin D. P., Callahan M. P., Dworkin J. P., Wu Q., Zare R. N., Grady M., Verchovsky S., Emel'yanenko V., Naroenkov S., Clark D. L., Girten B., and Worden P. S. 2014. Fall, recovery and characterization of the Novato L6 Chondrite Breccia. *Meteoritics & Planetary Science* 49:1388–1425.

Kita N. T., Welten K. C., Valley J. W., Spicuzza M. J., Nakashima D., Tenner T. J., Ushikubo T., MacPherson G. J., Welzenbach L., Heck P. R., Davis A., Caffee M. W., Laubenstein M., and Nishiizumi K. 2013. Fall, classification, and exposure history of the Mifflin L5 chondrite. *Meteoritics & Planetary Science* 48: 641–655.

Kohman T. P. and Bender M. L. 1967. Nuclide production by cosmic rays in meteorites and on the Moon. In *High-energy nuclear reactions in astrophysics—A collection of articles*, edited by Shen B. S. P. New York: W. A. Benjamin Inc. pp. 169–245.

Korochantseva E. V., Trieloff M., Lorenz C. A., Buykin A. I., Ivanova M. A., Schwarz W. H., Hopp J., and Jessberger E. K. 2007. L-chondrite asteroid breakup tied to Ordovician meteorite shower by multiple isochron ^{40}Ar-^{39}Ar dating. *Meteoritics & Planetary Science* 42:113–130.

Leya I. 2015. Data from the Noble Gas Cosmochemistry group at the University of Bern, Switzerland. Website: http://archive.space.unibe.ch/noblegas/data.html. Last accessed November 30, 2017.

Leya I. and Masarik J. 2009. Cosmogenic nuclides in stony meteorites revisited. *Meteoritics & Planetary Science* 44:1061–1086.

Li S. and Hsu W. 2016. U-Pb dating of the shock melt veins in two L6 chondrites. 79th Annual Meeting of the Meteoritical Society, 7–12 Aug, 2016, Berlin, Germany, A6057.

Li S. J., Leya I., Wang S. J., and Smith T. 2016. Cosmic-ray exposure ages of chondrites collected in Grove Mountains, Antarctica. 79th Annual Meeting of the Meteoritical Society, 7–12 Aug, 2016, Berlin, Germany, A6356.

Li Q.-L., Li X.-H., Liu Y., Tang G.-Q., Yang J.-H., and Zhu W.-G. 2010. Precise U-Pb and Pb-Pb dating of phanerozoic baddeleyite by SIMS with oxygen flooding technique. *Journal of Analytical Atomic Spectrometry* 25:1107–1113.

Llorca J., Trigo-Rodríguez J. M., Ortiz J. L., Docobo J. A., García-Guinea J., Castro-Tirado A. J., Rubin A. E., Eugster O., Edwards W., Laubesntein M., and Casanova

I. 2005. The Villalbeto de La Peña meteorite fall: I. Fireball energy, meteorite recovery, strewn field, and petrography. *Meteoritics & Planetary Science* 40:795–804.

Lodders K. 2003. Solar system abundances and condensation temperatures of the elements. *The Astrophysical Journal* 591:1220–1247.

Lodders K., Palme H., and Gail H. P. 2009. Abundances of the elements in the solar system. In *Solar system*, edited by Truemper J. E. Berlin, Germany: Springer. pp. 560–630.

Ludwig K. R. 1998. On the treatment of concordant uranium-lead ages. *Geochimica et Cosmochimica Acta* 62:665–676.

Mahajan R. R., Varela M. E., and Joron J. L. 2016. Santa Lucia (2008) (L6) chondrite, a recent fall: Composition, noble gases, nitrogen and cosmic ray exposure age. *Earth, Moon, and Planets* 117:65–76.

Marti K. and Graf T. 1992. Cosmic-ray exposure history of ordinary chondrites. *Annual Review of Earth and Planetary Sciences* 20:221–243.

McGraw A. M., Reddy V., and Sanchez J. A. 2017. Do L-chondrites come from the Gefion asteroid family? (abstract #1778). 48th Lunar and Planetary Science Conference. CD-ROM.

Meier M. M. M., Welten K. C., Riebe M. E., Riebe I., Caffee M. W., Gritsevich M., Maden C., and Busemann H. 2017. Park Forest (L5) and the asteroidal source of shocked L chondrites. *Meteoritics & Planetary Science* 52:1561–1576.

Nesvorný D., Morbidelli A., Vokrouhlický D., Bottke W. F., and Broz M. 2002. The Flora family: A case of the dynamically dispersed collisional swarm? *Icarus* 157: 155–172.

Nesvorný D., Vokrouhlický D., Morbidelli A., and Bottke W. F. 2009. Asteroidal source of L chondrite meteorites. *Icarus* 200:698–701.

Ostrowski D. R. and Bryson K. L. 2016. Physical properties comparison of ordinary chondrite classes. 79th Annual Meeting of the Meteoritical Society, 7–12 Aug, 2016, Berlin. LPI Contribution No. 1921, id. 6510.

Popova O. P., Jenniskens P., Emel'yanenko V., Kartashova A., Biryukov E., Khaibrakhmanov S., Shuvalov V., Rybnov Y., Dudorov A., Grokhovsky V. I., Badyukov D. D., Yin Q.-Z., Gural P. S., Albers J., Granvik M., Evers L. G., Kuiper J., Kharlamov V., Solovyov A., Rusakov Y. S., Korotkiy S., Serdyuk I., Korochantsev A. V., Larionov M. Y., Glazachev D., Mayer A. E., Gisler G., Gladkovsky S. V., Wimpenny J., Sanborn M. E., Yamakawa A., Verosub K., Rowland D. J., Roeske S., Botto N. W., Friedrich J. M., Zolensky M., Le L., Ross D., Ziegler K., Nakamura T., Ahn I., Lee J. I., Zhou Q., Li X.-H., Li Q.-L., Liu Y., Tang G.-Q., Hiroi T., Sears D., Weinstein I. A., Vokhmintsev A. S., Ishchenko A. V., Schmitt-Kopplin P., Hertkorn N., Nagao K., Haba M. K., Komatsu M., and Mikouchi T. 2013. Chelyabinsk airburst, damage assessment, meteorite recovery, and characterization. *Science* 342:1069–1073.

Rochette P., Gattacceca J., and Lewandrowski M. 2012. Magnetic classification of meteorites and application to the Soltmany fall. *Meteorites* 2:67–71.

Rubin A. E. 1990. Kamacite and olivine in ordinary chondrites: Intergroup and intragroup relationships. *Geochimica et Cosmochimica Acta* 54:1217–1232.

Sano Y., Oyama T., Terada K., and Hidaka H. 1999. Ion microprobe U-Pb dating of apatite. *Chemical Geology* 153:249–258.

Schmitz B., Tassinari M., and Peucker-Ehrenbrink B. 2001. A rain of ordinary chondritic meteorites in the early Ordovician. *Earth and Planetary Science Letters* 194:1–15.

Schmitz B., Yin Q.-Z., Sanborn M. E., Tassinari M., Caplan C. E., and Huss G. R. 2016. A new type of solar system material recovered from Ordovician marine limestone. *Nature Communications* 7:11,851–11,858.

Scott E. R. D. 2002. Meteorite evidence for the accretion and collisional evolution of asteroids. In *Asteroids III*, edited by Bottke W., Cellino A., Paolicchoi P., and Binzel R. Tucson, Arizona: The University of Arizona Press. pp. 697–709.

Shima M., Okada A., and Nagao K. 1993. The chondrite Mihonoseki: New observed fall. Proceedings, 24th Lunar and Planetary Science Conference. pp. 1297–1298.

Simon S. B., Grossman L., Clayton R. N., Mayeda T. K., Schwade J. R., Sipiera P. P., Wacker J. F., and Wadhwa M. 2004. The fall, recovery, and classification of the Park Forest meteorite. *Meteoritics & Planetary Science* 39:625–634.

Spergel M. S., Reedy R. C., Lazareth O. W., Levy P. W., and Slatest L. A. 1986. Cosmogenic neutron-capture-produced nuclides in stony meteorites. Proceedings, 16th Lunar and Planetary Science Conference. *Journal of Geophysical Research Supplement* 91:D483–D494.

Spoto F., Milani A., and Knezevic Z. 2015. Asteroid family ages. *Icarus* 257:275–289.

Stacey J. S. and Kramers J. D. 1975. Approximation of terrestrial lead isotope evolution by a two-stage model. *Earth and Planetary Science Letters* 26:207–221.

Stöffler D., Keil K., and Scott E. R. D. 1991. Shock metamorphism of ordinary chondrites. *Geochimica et Cosmochimica Acta* 55:3845–3867.

Takaoka N., Wakabayashi F., Shima M., and Wakabayashi F. 1989. Noble gas record of Japanese chondrites. *Z. Naturforshung* 44a:935–944.

Tatsumoto M., Knight R. J., and Allegre C. J. 1973. Time differences in the formation of meteorites as determined from the ratio of Lead-207 to Lead-206. *Science* 180:1279–1283.

Trigo-Rodriquez J. M., Llorca J., Weyrauch M., Bischoff A., Moyano-Cambero C. E., Keil K., Laubenstein M., Pack A., Madiedo J. M., Alonso-Azcárate J., Riebe M., Wieler R., Ott U., Tapia M., and Mestres N. 2014. Ardón: A long hidden L6 chondrite fall. 77th Annual Meeting of the Meteoritical Society, id. 5068.

Trinquier A., Birck J.-L., and Allègre C. J. 2007. Widespread ^{54}Cr heterogeneity in the inner solar system. *The Astrophysical Journal* 655:1179–1185.

Troiano J., Rumble D. III, Rivers M. L., and Friedrich J. M. 2011. Compositions of three low-FeO ordinary chondrites: Indications of a common origin with the H chondrites. *Geochimica et Cosmochimica Acta* 75:6511–6519.

Trotter J. A. and Eggins S. M. 2006. Chemical systematics of conodont apatite determined by laserablation ICPMS. *Chemical Geology* 223:196–216.

Vernazza P., Zanda B., Binzel R. P., Hiroi T., DeMeo F. E., Birlan M., Hewins R., Ricci L., Barge P., and Lockhart M. 2014. Multiple and fast: The accretion of ordinary chondrite parent bodies. *The Astrophysical Journal* 791:120–142.

Wasson J. T. 2012. *Meteorites: Classification and properties*, 2nd ed. London, UK: Springer. 205 p.

Wasson J. T. and Kallemeyn G. W. 1988. Compositions of chondrites. *Philosophical Transactions of the Royal Society of London Series A, Mathematical and Physical Sciences* 325:535–544.

Weirich J. R., Swindle T. D., Isachsen C. E., Sharp T. G., Li C., and Downs R. T. 2012. Source of potassium in shocked ordinary chondrites. *Geochmicia et Cosmochimica Acta* 98:125–139.

Welten K. C., Nishiizumi K., and Caffee M. W. 2001. The search for meteorites with complex exposure histories among ordinary chondrites with low 3He/21Ne ratios (abstract #2148). 32nd Lunar and Planetary Science Conference. CD-ROM.

Welten K. C., Nishiizumi K., Finkel R. C., Hillegonds D. J., Jull A. J. T., Franke L., and Schultz L. 2004. Exposure history and terrestrial ages of ordinary chondrites from the Dar al Gani region, Libya. *Meteoritics & Planetary Science* 39:481–498.

Welten K. C., Caffee M. W., and Nishiizumi K. 2016. The complex cosmic ray exposure history of Jesenice (L6): Possible evidence for ejection from parent body by tidal disruption or YORP related effects (abstract #2924). 47th Lunar and Planetary Science Conference. CD-ROM.

Wendt I. 1989. Geometric considerations of the three dimensional U/Pb data presentation. *Earth and Planetary Science Letters* 94:231–235.

Wendt I. and Carl C. 1984. U/Pb dating of discordant 0.1 Ma old secondary U minerals. *Earth and Planetary Science Letters* 73:278–284.

Wu Y. and Hsu W. 2017. Petrology, mineralogy and in situ U-Pb dating of Northwest Africa 11042. 80th Annual Meeting of the Meteoritical Society (LPI Contribution Number 1987) A6190.

Yamakawa A., Yamashita K., Makishima A., and Nakamura E. 2009. Chemical separation and mass spectrometry of Cr, Fe, Ni, Zn, and Cu in terrestrial and extraterrestrial materials using thermal ionization mass spectrometry. *Analytical Chemistry* 81:9787–9794.

Yin Q.-Z., Zhou Q., Li Q.-L., Li X.-H., Liu Y., Tan G.-Q., Krot A. N., and Jenniskens P. 2014. Records of the Moon-forming impact and the 470 Ma disruption of the L chondrite parent body in the asteroid belt from U-Pb apatite ages of Novato (L6). *Meteoritics & Planetary Science* 49:1426–1439.

Youdin A. N. 2011. On the formation of planetesimals via secular gravitational instabilities with turbulent stirring. *The Astrophysical Journal* 731:99–117.

Zhou Q., Ying Q.-Z., Edward D. Y., Li X.-H., Wu F.-Y., Li Q.-L., Liu Y., and Tang G.-Q. 2013. SIMS Pb-Pb and U-Pb age determination of eucrite zircons at <5 micron scale and the first 50 Ma of the thermal history of Vesta. *Geochimica et Cosmochimica Acta* 110:152–175.